Gold mineralized diorite beneath the Linglong ore field, North China Craton: New insights into the origin of decratonization-related gold deposits

Zhan-Ke Li[1, 2†], Jian-Wei Li[1, 2], Hua-Shan Sun[1], Xin-Fu Zhao[1, 2], Andrew G. Tomkins[3], David Selby[4], Paul T. Robinson[1, 2], Xiao-Dong Deng[2], Zaicong Wang[2, 5], Zhong-Zheng Yuan[1], and Shao-Rui Zhao[1]

[1]*School of Earth Resources, China University of Geosciences, Wuhan 430074, China*

[2]*State Key Laboratory of Geological Processes and Mineral Resources, China University of Geosciences, Wuhan 430074, China*

[3]*School of Earth, Atmosphere and Environment, Monash University, Melbourne, Victoria 3800, Australia*

[4]*Department of Earth Sciences, University of Durham, Durham DH1 3LE, United Kingdom*

[5]*School of Earth Sciences, China University of Geosciences, Wuhan 430074, China*

† Corresponding author: lizk@cug.edu.cn

ABSTRACT

Gold deposits in Precambrian cratons were mostly generated during the formation and stabilization of the cratons, but the North China Craton (NCC) is unusual in that its gold deposits were mainly formed ca. 1.7 billion years after its stabilization. A magmatic-hydrothermal origin or mantle-derived fluid source has been proposed for the giant gold deposits of the Jiaodong district in the eastern NCC, but direct evidence is sparse and the mineralization processes remain controversial. Here, we present the results of a comprehensive geological, geochronological, and geochemical study of the gold mineralized Xiejia diorite beneath the Linglong ore field at Jiaodong to link the gold mineralization to underlying magmatism. Magmatic zircon and titanite grains from the Xiejia diorite have LA-ICP-MS U-Pb ages of 121.3 ± 0.9 Ma to 120.8 ± 1.1 Ma and 121.7 ± 3.9 Ma, respectively, which are indistinguishable from the time of gold deposition throughout the Jiaodong district as constrained by previous studies. The diorite has a shoshonitic composition and is characterized by strong enrichment in large-ion lithophile elements (LILE) and light rare earth elements (LREE) along with significant depletion in high-field-strength elements (HFSE) and heavy rare earth elements (HREE). Samples of the diorite have high initial $^{87}Sr/^{86}Sr$ ratios, but low $\varepsilon_{Nd}(t)$ and $\varepsilon_{Hf}(t)$ values and low Pb isotope ratios. These geochemical characteristics are akin to those of contemporaneous mafic dikes in most gold mines at Jiaodong, indicating that the Xiejia diorite was most likely derived from an enriched lithospheric mantle source. The upper part of the diorite intrusion is pervasively altered and mineralized, containing an average of 0.32 g/t Au but locally up to 7.59 g/t. Hydrothermal titanite from the mineralized diorite has a LA-ICP-MS U-Pb age of 122.3 ± 4.3 Ma, which is consistent with the gold-bearing pyrite Re-Os isochron age of 122.5 ± 6.7 Ma. Ore-related sericite aggregates from the Dongfeng gold deposit above the Xiejia diorite have an $^{40}Ar/^{39}Ar$ plateau age of 122.6 ± 1.3 Ma. Pyrite from the mineralized diorite yielded $\delta^{34}S_{CDT}$ values of 2.1 to 9.7 ‰, which are comparable with those of pyrite ($\delta^{34}S_{CDT}$ = 5.8 to 8.1 ‰) from gold ores of Dongfeng. Pyrite grains from both groups also have similar Pb isotope compositions. The sulfur and lead isotope data are consistent with values of mafic dikes which are spatially and temporally associated with gold

veins in the Linglong ore field. The results presented here thus indicate a possible genetic link between gold mineralization in the Xiejia diorite and underlying magma presumably represented by the Xiejie diorite. The auriferous fluids exsolved from that magma migrated upwards along the Potouqing Fault to form the Dongfeng gold deposit above the Xiejia diorite. The mineralized diorite thus links shallow gold mineralization to deep-seated mantle-derived magmatism generated during the extensive destruction of the NCC induced by the rollback of the subducted Paleo-Pacific plate.

INTRODUCTION

The Jiaodong gold province in the eastern NCC contains proven gold reserves of more than 5,000 tons, being the largest gold producer in China and one of the largest gold provinces in the world (Li et al., 2003; Goldfarb and Santosh, 2014; Groves and Santosh, 2016; Deng et al., 2020a; Zhang et al., 2020). Available geochronological data reveal that gold mineralization throughout the Jiaodong province occurred at ca. 120 Ma (Yang and Zhou, 2001; Li et al., 2003, 2006; Yuan et al., 2019; Zhang et al., 2020), ca. 1.7 billion years after high-grade regional metamorphism associated with the formation and stabilization of the NCC (Zhao et al., 2001; Jahn et al., 2008; Goldfarb and Santosh, 2014). Although gold deposits over the district have been extensively studied, gold source and ore genesis remain hotly debated (Goldfarb and Santosh, 2014; Zhu et al., 2015; Deng et al., 2020a; Groves et al., 2020). Mesozoic granitoid intrusions are widespread at Jiaodong and host a major part of gold resources (Fig. 1). The granitoid magmatism occurred mainly in the 160-150 Ma and 130-126 Ma intervals (e.g., Wang et al., 1998; Hou et al., 2007; Xu et al., 2022), predating the gold mineralization by 6 to 40 Myrs. Thus, neither the Precambrian high-grade metamorphic basement rocks nor the

Mesozoic granitoid intrusions have largely contributed to the giant gold deposits at Jiaodong (Goldfarb and Santosh, 2014; Wang et al., 2021; Xu et al., 2022).

Mafic to intermediate dikes are widespread in most gold mines at Jiaodong and have close spatial relations to ore bodies (Yang et al., 2004; Tan et al., 2012; Zhu et al., 2020). Geochronological studies have shown that these dikes formed between 135 Ma to 108 Ma (Yang et al., 2004; Liu et al., 2009; Deng et al., 2017; Wang et al., 2020a; Koua et al., 2022), broadly coeval with gold deposition and the peak of lithospheric destruction of the NCC (Zhu et al., 2011, 2021; Yang et al., 2021). This temporal and spatial relationship strongly suggests that both the gold and ore fluids were likely sourced from deep-seated magmatism triggered by the lithospheric destruction (Li et al., 2003; Zhu et al., 2012, 2015; Wang et al., 2020b). This view is partly supported by a large collection of stable and noble gas isotope data (Fan et al., 2003; Mao et al., 2008; Li et al., 2012; Tan et al., 2018; Deng et al., 2020b). However, some researchers suggest that the auriferous fluids were mostly derived from devolatilization of the subducting Paleo-Pacific slab or an enriched mantle source above the slab (Goldfarb and Santosh, 2014; Groves and Santosh, 2016; Groves et al., 2020). Nevertheless, direct geological evidence remains scarce for either model. Most notably, no causal intrusive bodies have been documented to support the magmatic hydrothermal model.

Recent prospective drilling in the Linglong ore field at Jiaodong, which reached depths of more than 2000 m below the present surface, revealed pervasive gold mineralization in the unexposed Xiejia diorite (Shandong Zhaojin Group Co. LTD, 2015). This discovery provided an ideal opportunity to examine a possible genetic relationship between gold mineralization and magmatism in this ore field. Here we present zircon LA-ICP-MS U-Pb ages, whole-rock major and trace element data, and Sr-Nd-Hf-Pb isotopic compositions of the diorite to constrain its petrogenesis. We then use titanite U-Pb, pyrite Re-Os, and sericite $^{40}Ar/^{39}Ar$ isotopes to constrain the timing of the gold mineralization and its temporal relationship to the Xiejia diorite. Lastly, we use pyrite S and Pb isotope data to provide information on the source of sulfur and other components in the ore fluids. These results, when combined with previously published data, support a genetic link between the magmas derived from the enriched lithospheric mantle of the NCC and gold mineralization in the Jiaodong province.

GEOLOGICAL BACKGROUND

The NCC contains crustal rocks as old as 3.8 Ga (Liu et al., 1992). It consists of the Eastern and Western Blocks separated by the Trans-North China Orogen (TNCO), which was produced by a collisional event at ca. 1.85 Ga (Zhao et al., 2001; Fig. 1). This collision led to the final amalgamation and stabilization of the NCC (Zhao et al., 2001, 2005). Shallow-marine carbonate platform sediments accumulated on the craton from the late Paleoproterozoic to the end of the Paleozoic (Yang et al., 1986), whereas multiple Paleozoic to early Mesozoic orogenic events occurred along its northern and southern margins (Xiao et al., 2003, 2015; Zhai, 2010; Dong et al., 2011). Late Mesozoic metamorphic core complexes, rift basins, A-type granites, and bimodal volcanic rocks are widely developed in the eastern NCC, which are interpreted as the results of extensional tectonism associated with lithospheric destruction of the NCC (Tian et al., 1992; Ren et al., 2002; Zhu et al., 2010; Charles et al., 2012). The destruction of the NCC was probably induced by the rollback of the subducted Paleo-Pacific plate along the eastern Asian margin during the Early Cretaceous (Wu et al., 2005; Zhu et al., 2012, 2015).

The Jiaodong gold province is composed mainly of Precambrian metamorphic rocks that are intruded by large volumes of Mesozoic granitoid intrusions and extensively covered by terrestrial sedimentary rocks of Cretaceous to Cenozoic ages (Fig. 1). The Precambrian rocks include the Neoarchean Jiaodong Group, the Paleoproterozoic Fenzishan and Jinshan Groups, and the Meso-Neo-proterozoic Penglai Group. The Jiaodong Group consists chiefly of TTG (tonalite-trondhjemite-granodiorite) gneiss and amphibolitic gneiss, whereas the Fenzishan and Jinshan Groups are composed predominantly of amphibolite facies metasedimentary rocks, and the Penglai Group consists of metasedimentary rocks (SBGMR, 1991; Tang et al., 2007; Deng et al., 2020b). Zircon U-Pb dating results have revealed two major magmatic and metamorphic events at 2.52-2.41 Ga and 2.22-1.81 Ga (Zhao et al., 2001; Jahn et al., 2008; Zhou et al., 2008).

The Mesozoic granitoid intrusions include the Late Jurassic Linglong suite that comprises the Linglong biotite granite and Luanjiahe monzogranite with zircon U-Pb ages of 160-150 Ma, the middle Early Cretaceous Guojialing suite that is dominated by granodiorite emplaced at 130-126 Ma, and the late Early Cretaceous Aishan suite that consists of the Aishan and Yashan monzogranites dated at 118-113 Ma (Fig. 1; Wang et al., 1998; Hou et al., 2007; Goss et al., 2010; Yang et al., 2012a). Petrological and geochemical data, along with the presence of abundant inherited zircons, indicate that the Linglong suite was generated by partial melting of ancient lower-crustal rocks at depths >50 km, whereas the Guojialing suite was formed by mixing of eclogite-derived melts, crustal melts, and melts derived from upwelling asthenospheric mantle (Yang et al., 2003; Hou et al., 2007; Yang et al., 2012a). In contrast, the Aishan suite resulted from partial melts of lower crustal rocks that subsequently mixed with upper mantle-derived materials (Hou et al., 2007; Yang et al., 2012b).

Abundant mafic, intermediate, and felsic dike swarms are widespread in the Jiaodong province, with zircon U-Pb ages ranging from 135 Ma to 108 Ma (Yang and Zhou, 2001; Liu et al., 2009; Deng et al., 2017; Wang et al., 2020a). Most of the mafic dikes are enriched in LILEs and LREEs but depleted in HFSEs, suggesting an enriched lithospheric mantle source (Liu et al., 2009; Cai et al., 2015; Long et al., 2017; Wang et al., 2020a). Early Cretaceous volcanic rocks and Cenozoic sedimentary rocks locally overlie both Precambrian basement rocks and Mesozoic intrusions (Fig. 1; Xie et al., 2012). The volcanic rocks, which comprise a bimodal mafic-silicic suite, are considered to represent melt products of enriched lithospheric mantle and ancient lower crust (Ling et al., 2009; Kuang et al., 2012).

The Jiaodong province is structurally dominated by a group of NNE- to NE-trending faults, which are considered to be secondary and higher-order structures of the continental Tan-Lu Fault zone (Fig. 1). These faults were originally formed during the Jurassic and then reactivated in the Early Cretaceous (Deng et al., 2003, 2015). Minor NW-trending faults locally crosscut the NNE- to NE-trending features (Yang et al., 2014). Most of the gold deposits are distributed along the Sanshandao, Jiaojia, and Zhaoping Faults, which mostly developed along favorable lithologic contacts, such as between igneous and metamorphic rocks or between different igneous bodies (Figs. 1, 2). Gold mineralization throughout the province consists mainly of quartz-sulfide±carbonate veins and sulfide disseminations and veinlets in hydrothermally altered magmatic rocks (e.g., Li et al., 2006; Deng et al., 2020a; Qiu et al., 2022).

GEOLOGY OF THE LINGLONG ORE FIELD

The Linglong ore field is the second largest gold concentration in Jiaodong (Fig. 1) and is lithologically dominated by the Linglong biotite granite and Luanjiahe monzogranite, which intruded the Neoarchean metamorphic rocks of the Jiaodong Group between 159 ± 2 to 153 ± 4 Ma as constrained by zircon U-Pb dating (Fig. 2A; Wang et al., 1998; Yang et al., 2012a). The Early Cretaceous Guojialing granodiorite (ca. 130 Ma; Wang et al., 1998; Yang et al., 2012a) occurs mostly in the northwestern and northeastern parts of the ore field (Fig. 2A).

The Linglong ore field is structurally dominated by the Potouqing Fault, which separates the Linglong biotite granite to the northwest from the Luanjiahe monzogranite to the southeast (Fig. 2). This fault zone, which is more than 15 km long and 40-320 m wide, strikes 40°-80° NE, and dips 28°-47° SE. Granitic rocks near the fault zone were subjected to intensive deformation to form cataclasite or mylonite. Granitic cataclasite, mylonite, and fault gouge within the fault zone are overprinted by broad zones of hydrothermal alteration (Fig. 2B). The Linglong Fault strikes 20°-25° NE, dips 65°-85° SE, and cuts through the Linglong biotite granite and the Potouqing Fault. The NE-trending Jiuqu-Jiangjia Fault is developed on the footwall of the Potouqing Fault.

Mafic to intermediate dike swarms are common in the ore field, particularly within the Linglong biotite granite (Fig. 2A). These dikes, mainly consisting of quartz diorite porphyry, diorite porphyry, and lamprophyre, have whole-rock K-Ar and zircon U-Pb ages of 123.9 ± 2.5 Ma to 122.3 ± 4.3 Ma (Yang et al., 2004; Long et al., 2017). Most of the dikes are accommodated in the NE-trending faults where they are spatially and temporally associated with gold veins (Fig. 2A). The mafic to intermediate dikes are enriched in LILEs and LREEs and depleted in the HFSEs. They also have relatively high initial $^{87}Sr/^{86}Sr$ ratios and low $\varepsilon_{Nd}(t)$ values, suggesting derivation from an enriched mantle source (Yang et al., 2004; Long et al., 2017; Wang et al., 2020a).

More than 1,000 t of gold resources have been discovered in this ore field, with about half having been mined (Yang et al., 2016; Liu et al., 2019). Several hundreds of gold veins are hosted in the Linglong granite, where they are controlled by NE-trending faults in the footwall of the Potouqing Fault. Gold mineralization consists of quartz-sulfide±carbonate veins and sulfide disseminations in hydrothermally altered granite, both being strictly controlled by the faults. The quartz-sulfide±carbonate veins are best represented by the Xishan, Dongshan, and Jiuqu deposits, which are hosted by the Linglong and Jiuqu-Jiangjia Faults and associated secondary structures (Fig. 2A). The mineralized alteration assemblages are mostly developed within the Potouqing Fault, with the Taishang, Dongfeng, and Shuiwangzhuang deposits being the major examples (Fig. 2A; Yang et al., 2016; Liu et al., 2019).

GOLD MINERALIZATION IN THE XIEJIA DIORITE

The Xiejia diorite beneath the Linglong ore field has been revealed by deep drilling in the Luanjiahe area (Shandong Zhaojin Group Co. LTD, 2015; Shen et al., 2016). Two diamond drill holes (DDH) encountered the Xiejia diorite at depths of 2065 to 2195 m for DDH72-ZK1, and 2329 m and 2392 m for DDH84-ZK1, but neither of them penetrated the diorite intrusion (Fig. 2B). The Potouqing Fault was intersected in the two drill holes at less than 200 m above the Xiejia diorite (Fig. 2B), and is inferred to connect with the diorite along its downward direction. A representative drill hole with geological log and gold concentration data is shown in Supplemental Figure S1.

The Xiejia diorite is medium-grained (Fig. 3A-C) and composed chiefly of plagioclase (25-40 modal %), biotite (15-30 %), alkali feldspar (10-20 %), amphibole (5-15 %), and quartz (5 %) (Fig. 4A), with accessory magnetite, titanite, and zircon. The diorite penetrated by both drill holes exhibits pervasive hydrothermal alteration, especially in the uppermost parts of the intrusion (Fig. 3C), with chlorite, sericite, titanite, and calcite being the major alteration phases (Fig. 4B-C). Coarse-grained calcite commonly occurs in miarolitic cavities within the diorite, and epidote veins are present locally (Fig. 4D).

Both magmatic and hydrothermal titanite are common in the diorite (Fig. 5). Magmatic grains are euhedral to subhedral, mostly 200 to 500 μm long, and display core-rim textures in BSE images (Fig. 5A-B); these grains generally coexist with amphibole and plagioclase. Hydrothermal titanite is closely associated with Au-bearing pyrite, chlorite, quartz, and calcite (Fig. 5C-F), and is divided into two sub-types. Type 1 titanite grains have irregular shapes and patchy textures in BSE images (Fig. 5C-D), whereas Type 2 titanite varieties show strong evidence of hydrothermal metasomatism and are associated with secondary rutile and bastnaesite (REE mineral) (Fig. 5E-F).

Bulk-rock analyses show that the Xiejia diorite is enriched in gold (Fig. 2B, Supplemental Fig. S1). Specifically, most dioritic samples from drill hole 72-ZK1 are mineralized and contain detectable gold (>0.05 g/t), with grades up to 7.6 g/t Au between 2114.56 and 2115.56 m, and possessing an average of 0.32 g/t Au between 2065 and 2195 m (Supplemental Fig. S1). Sulfide minerals are abundant in the altered diorite (locally up to 5 vol.%) (Fig. 3A-C), and mostly occur as disseminations or interstitial infillings between the rock-forming minerals (Figs. 3A-C, 6A-D). Pyrite is the most abundant sulfide mineral, locally associated with minor pyrrhotite and chalcopyrite. The sulfide minerals, along with chlorite and sericite, typically replace primary amphibole and plagioclase grains (Fig. 6A). Native gold occurs locally as infillings along microfractures in pyrite or as inclusions in quartz (Fig. 6B). The sulfide minerals are typically intergrown with other hydrothermal minerals including quartz, calcite, and titanite (Fig. 6B-D).

Hydrothermal alteration is also pervasive along the Potouqing Fault zone above the Xiejia diorite (Fig. 2B, Supplemental Fig. S1). The alteration phases are dominated by potassic feldspar, sulfides, quartz, and sericite (Fig. 3D). Two orebodies (No. 2-2-6 and No. 2-1-3-1) in the alteration zone around the Potouqing Fault penetrated by drill hole 84-ZK1 have gold grades of 1.78 g/t and 1.50 g/t, respectively (Shandong Zhaojin Group Co. LTD, 2015), and these orebodies are deep extensions of the Dongfeng deposit (Fig. 2). Sulfide minerals in the mineralized alteration zone consist of pyrite, sphalerite, and galena (Figs. 3D, 6E-F), along with native gold included in pyrite or sphalerite (Fig. 6E). Sericite in the alteration zone is spatially related to the sulfide minerals (Fig. 6F).

SAMPLES AND ANALYTICAL METHODS

A total of 108 samples were collected from drill holes 72-ZK1 and 84-ZK1 for this study. Most samples are from the diorite intrusion, but some samples from the auriferous alteration zone along the Potouqing Fault were also collected (See Supplemental Table S1 for details of the representative samples; Fig. 2B). Polished thin sections from each sample were examined under the microscope to characterize their mineralogy, textures, and paragenesis. Whole-rock major oxides, trace elements, and Sr-Nd-Hf isotopes were determined for six diorite samples. Zircon grains extracted from two of those samples were dated using U-Pb isotopes by

LA-ICP-MS. Titanite grains in polished thin sections of the diorite were analyzed for major and trace element compositions, as well as U-Pb and Nd isotopes. Pyrite grains from seven mineralized diorite samples were selected for Re-Os dating, whereas sericite aggregates from an alteration assemblage along the Potouqing Fault were used for $^{40}Ar/^{39}Ar$ geochronology. Pyrite grains from the mineralized diorite and alteration zone of the Potouqing Fault were both selected for in situ S and Pb isotope analysis.

Whole-rock major and trace element analyses were carried out at the ALS Laboratory Group, Guangzhou, China. Whole-rock Sr-Nd-Hf isotope analyses, mineral U-Pb dating and elemental analyses were carried out at the Wuhan Sample Solution Analytical Technology Co. Ltd, China. Lead isotopic compositions of plagioclase and pyrite and sulfur isotopes of pyrite were determined using LA-ICP-MS at the State Key Laboratory of Geological Processes and Mineral Resources (GPMR), China University of Geosciences, Wuhan. Rhenium-Os isotopes were determined at the Laboratory for Sulfide and Source Rock Geochronology and Geochemistry, Durham University, UK by isotope-dilution negative thermal ionization mass spectrometry (ID-NTIMS). The $^{40}Ar/^{39}Ar$ dating of sericite was performed at the Key Laboratory of Tectonics and Petroleum Resources (TPR), Ministry of Education, China University of Geoscience, Wuhan. The detailed analytical methods are given in Supplemental Text S1.

RESULTS

Zircon and Titanite U-Pb ages

Thirty-nine and twenty-four spot analyses of zircon U-Pb isotopes were obtained for samples LJH41 and LJH66, respectively (Supplemental Table S2, Fig. S2). All spot analyses for sample LJH41 are concordant, with 13 spots forming a coherent group that yields a weighted mean LA-ICP-MS $^{206}Pb/^{238}U$ age of 121.3 ± 0.9 [± 2.2 including the systematic uncertainty] Ma (2σ, MSWD = 0.5) (Fig. 7A-B). The remaining 26 spot analyses have older LA-ICP-MS $^{206}Pb/^{238}U$ dates ranging from 2263 to 154 Ma, which are interpreted as inherited grains (Fig. 7A). Similarly, 12 spot analyses on zircon grains from sample LJH66 are concordant and yield a weighted mean LA-ICP-MS $^{206}Pb/^{238}U$ age of 120.8 ± 1.1 [± 2.3 including the systematic uncertainty] Ma (2σ, MSWD = 0.3) (Fig. 7C-D). The remaining analyses are also concordant or marginally concordant, with $^{206}Pb/^{238}U$ dates ranging from 871 to 157 Ma that are interpreted as inherited grains. The U-Pb dating suggests that the Xiejia diorite was emplaced at ca. 120 Ma.

U-Pb isotope data of titanite are presented in Supplemental Table S3 and shown in Supplemental Figure S3. Twenty-three spot analyses on magmatic titanite define a lower intercept LA-ICP-MS age of 121.7 ± 3.9 [± 4.4 including the systematic uncertainty] Ma (2σ, MSWD = 0.3) in the Tera-Wasserburg diagram, with a Y-intercept of common $^{207}Pb/^{206}Pb$ at 0.810 ± 0.060 (Fig. 7E). In comparison, the lower intercept LA-ICP-MS age of hydrothermal titanite is 122.3 ± 4.3 [± 4.8 including the systematic uncertainty] Ma (2σ, MSWD = 0.3) with a Y-intercept of common $^{207}Pb/^{206}Pb$ composition at 0.800 ± 0.030 (Fig. 7F).

Pyrite Re-Os and sericite $^{40}Ar/^{39}Ar$ dates

Total Re abundances in pyrite grains of seven samples range from 0.75 to 1.50 ppb, whereas Os abundances are from 2.18 to 13.52 ppt (Supplemental Table S4). Radiogenic Os ($^{187}Os^{r}$) dominates the osmium budget for the majority of the samples, and as a result the blank for ^{188}Os comprises a significant component of the measured value (16.7-62.5 %). The samples have $^{187}Re/^{188}Os$ ratios of 361 to 4648 (mostly between 1070 and 4648); they also have radiogenic $^{187}Os/^{188}Os$ compositions (1.4 to 9.2) and exhibit highly correlated uncertainties (rho = 0.298 to 0.995, mostly between 0.945 and 0.995). Collectively, the $^{187}Re/^{188}Os$, $^{187}Os/^{188}Os$, and rho data yielded a Model 3 Re-Os date of ca. 114.5 ± 13.2 Ma with an initial $^{187}Os/^{188}Os$ of 0.52 ± 0.68 ($^{187}Os/^{188}Os$ dispersion 0.38 + 0.38 / - 0.16; 2σ, MSWD = 11; Fig. 8A). The Re-Os data exhibit considerable scatter (overdispersion) about the linear regression, which is masked by the error correlation in a conventional isochron diagram, but is more clearly visible on an inverse $^{187}Re/^{187}Os$ versus $^{188}Os/^{187}Os$ isochron plot, whereby the imprecise values (those with highly correlated errors) no longer dominate the plot (Fig. 8B; Li and Vermeesch, 2021). The Re-Os data for three samples (LJH48, LJH61-1, and LJH61-2) yielded a Model 1 Re-Os date of 122.5 ± 6.7 [± 6.8 including the decay constant] Ma with an initial $^{187}Os/^{188}Os$ of 0.66 ± 0.19 (2σ, MSWD = 0.005; Fig. 8C), which is consistent with the inverse isochron age of 122.5 ± 6.8 Ma (2σ, MSWD = 0.005; Fig. 8D).

The $^{40}Ar/^{39}Ar$ dating results for the hydrothermal sericite from sample LJH109 are summarized in Supplemental Table S5. The sample yielded a plateau age of 122.6 ± 1.3 Ma (2σ, MSWD = 2.4), consisting of five contiguous steps that account for 60 % of the total ^{39}Ar released (Fig. 9A). The spectra are characterized by young apparent ages in the initial several steps, which reflect minor argon loss after crystallization of the sericite (e.g., Li et al., 2006). Partial argon loss is also implied by the integrated age, which is ca. 1 Myr younger than the corresponding plateau age (Fig. 9A). The argon loss from the sericite may have been caused by later tectonothermal events associated with the evolution of the Linglong metamorphic core complex (Wu et al., 2020). The plateau-age steps form a well-defined isochron in the $^{39}Ar/^{40}Ar$

versus $^{36}Ar/^{40}Ar$ diagram (Fig. 9B), with an isochron age of 121.3 ± 2.8 Ma (2σ, MSWD = 1.9) that is indistinguishable within uncertainty from the plateau age.

Major and trace element compositions of whole-rock diorite samples

Diorite samples commonly have large loss on ignition (LOI) ranging from 3.56 to 7.39 wt.% (Supplemental Table S6), which reflects the variable degrees of hydrothermal alteration (Fig. 4B-D). These samples contain 46.98-54.32 wt.% SiO_2 and 5.22-6.32 wt.% total alkalis (Na_2O + K_2O), and plot in the fields of gabbro and syeno-diorite in the SiO_2 vs. (Na_2O + K_2O) diagram (Fig. 10A). In the Nb/Y vs. Zr/TiO_2 diagram (Fig. 10B), the rocks plot in the andesite and dacite fields. All the samples are shoshonitic and metaluminous (Fig. 10C-D), significantly enriched in LILEs, and depleted in HFSEs (Fig. 10E). The ΣREE contents of the samples range from 203 to 338 μg/g, and all samples are characterized by LREE enrichment relative to HREEs, with $(La/Yb)_N$ ratios of 15.8-37.5 (Fig. 10F) and weak Eu anomalies (0.85-1.04; $\delta Eu = 2[Eu]_N/([Sm]_N + [Gd]_N)$). The geochemical characteristics of the Xiejia diorite compare closely to those of the Early Cretaceous mafic dikes in the Linglong ore field and throughout Jiaodong province (Yang et al., 2004; Ma et al., 2016).

Whole-rock Sr-Nd-Hf and plagioclase Pb isotopes

Whole-rock Sr-Nd-Hf isotopes for the Xiejia diorite are listed in Supplemental Table S7. All samples show relatively uniform initial $^{87}Sr/^{86}Sr$ ratios of 0.70722 to 0.70780 at 120 Ma and have $\varepsilon_{Nd}(t)$ (t = 120 Ma) values of −13.2 to −14.7 (Fig. 11A). The samples have $^{176}Hf/^{177}Hf$ ratios of 0.28218 to 0.28225 that correspond to calculated $\varepsilon_{Hf}(t)$ (t = 120 Ma) values of −16.9 and −19.3 (Fig. 11B). Lead isotopic ratios of plagioclase are relatively uniform at

16.695-16.899 for $^{206}Pb/^{204}Pb$, 15.377-15.453 for $^{207}Pb/^{204}Pb$, and 36.949-37.198 for $^{208}Pb/^{204}Pb$ (Supplemental Table S8). They all plot above the Northern Hemisphere Reference Line (NHRL) in the $^{206}Pb/^{204}Pb$ vs. $^{207}Pb/^{204}Pb$ and $^{208}Pb/^{204}Pb$ diagrams (Fig. 11C-D).

Major and trace element compositions of titanite

Magmatic titanite from the Xiejia diorite (n = 23) contains 56.23-60.77 wt.% $CaO+TiO_2$ and 2.31-4.10 wt.% $Al_2O_3+Fe_2O_3$, whereas the hydrothermal variety (n = 19) has higher $CaO+TiO_2$ (60.83-63.83 wt.%) and lower $Al_2O_3+Fe_2O_3$ (1.97-3.13 wt.%) (Supplemental Table S9; Fig. 12A). The magmatic titanites have moderate to high concentrations of U (36-558 ppm), Th (94-964 ppm), Zr (210-5,114 ppm), Y (1,876-9,217 ppm), Nb (842-4,796 ppm), Ta (29-468 ppm), and ∑REEs (16,069-34,380 ppm; Fig. 12B). In chondrite-normalized REE patterns, they are characterized by large and variable LREE/HREE ratios (5.0-16.6) and $(La/Yb)_N$ ratios (4.1-16.6) (Fig. 12C), with negative Eu anomalies (0.35-0.64) and positive Ce anomalies (3.6-4.6) (Fig. 12D). In sharp contrast, the hydrothermal varieties contain much lower U (2.8-79 ppm), Th (7.3-500 ppm), Zr (37-3,008 ppm), ∑REEs (785-12,270 ppm), Y (209-2,605 ppm), Nb (26-1,432 ppm), and Ta (1.0-107 ppm) (Supplemental Table S9; Fig. 12B). In chondrite-normalized REE patterns, the hydrothermal titanite displays relatively low LREE/HREE ratios of 1.1-9.0 and $(La/Yb)_N$ ratios of 0.1-5.1 (Fig. 12C), with highly variable Eu anomalies (0.66-1.97) and weak positive Ce anomalies (2.1-3.8) (Fig. 12D). The gradual decrease in REEs (notably for LREEs) from magmatic titanite to its hydrothermal variety (Fig. 12B-C) suggests that the REEs might have been released to the hydrothermal fluids during the alteration of the magmatic titanite to form REE-rich minerals such as bastnaesite (Fig. 5E-F).

Nd isotopes of titanite

The measured $^{143}Nd/^{144}Nd$ ratios of magmatic titanite range from 0.511822 to 0.511902 (n = 10), which correspond to calculated $\varepsilon_{Nd}(t)$ (t = 120 Ma) values of −13.3 to −14.6. These values are indistinguishable from the $\varepsilon_{Nd}(t)$ values of the whole-rock diorite samples (Supplemental Table S10; Fig. 13A). Both type 1 and type 2 hydrothermal titanites show restricted $^{143}Nd/^{144}Nd$ values of 0.511833-0.511888 (n = 8) and 0.511835-0.511934 (n = 9), respectively. The calculated $\varepsilon_{Nd}(t)$ (t = 120 Ma) values are −13.5 to −14.5 for type 1 titanites and −12.8 to −14.7 for type 2 grains, consistent with those of the magmatic titanite and whole-rock samples of the Xiejia diorite (Fig. 13A).

In situ S and Pb isotopes of pyrite

Gold-bearing pyrite from the mineralized Xiejia diorite has $\delta^{34}S_{CDT}$ values ranging from 2.1 to 9.7 ‰ (mean of 5.3‰, n = 32), whereas grains from the auriferous hydrothermal alteration zone along the Potouqing Fault vary from 5.8 to 8.1 ‰ in $\delta^{34}S_{CDT}$ (mean of 7.2 ‰, n = 12) (Supplemental Table S11). The pyrite sulfur isotope data overlap those of gold deposits in the Linglong ore field (Fig. 13B).

The low contents of total Pb in pyrite from the Xiejia diorite led to large uncertainties in the Pb isotopic ratios, which are 16.989-17.413 for $^{206}Pb/^{204}Pb$, 15.386-15.649 for $^{207}Pb/^{204}Pb$), and 37.535-38.313 for $^{208}Pb/^{204}Pb$ (Supplemental Table S12). Pyrite from the alteration zone of the Potouqing Fault has $^{206}Pb/^{204}Pb$ ratios of 17.362-17.449, $^{207}Pb/^{204}Pb$ ratios of 15.460-15.483, and $^{208}Pb/^{204}Pb$ ratios of 37.931-38.042. There is no obvious difference in Pb isotope ratios between pyrite from the alteration zone of the Potouqing Fault and the gold deposits in the Linglong ore field (Fig. 13C-D).

DISCUSSION

Ages of the diorite intrusion and associated gold mineralization

Most of the zircon grains dated in this study have high Th/U ratios and are characterized by oscillatory zoning in CL images (Supplemental Table S2, Fig. S2), indicating a magmatic origin (Hoskin and Schaltegger, 2003). Thus, zircon LA-ICP-MS U-Pb dates obtained here (121.3 ± 0.9 Ma and 120.8 ± 1.1 Ma) are interpreted as the best estimate for the time of emplacement of the Xiejia diorite. This emplacement age is further confirmed by the LA-ICP-MS U-Pb date of 121.7 ± 3.9 Ma of the magmatic titanite (Fig. 7E).

Hydrothermal titanite associated with Au-bearing pyrite (Figs. 5C-D, 6B, D) yielded a LA-ICP-MS U-Pb age of 122.3 ± 4.3 Ma (Fig. 7F), which is interpreted as the time of disseminated gold mineralization in the Xiejia diorite. This age overlaps the pyrite Re-Os isochron age of 122.5 ± 6.7 Ma (Fig. 8A, C) and the sericite $^{40}Ar/^{39}Ar$ plateau age of 122.6 ± 1.3 Ma (Fig. 9A). The good agreement of the dating results by different methods confirms the reliability of the Re-Os and $^{40}Ar/^{39}Ar$ analyses when interpreted as the time of gold deposition, although both datasets are small. The similar ages of the ore mineral and associated alteration phases from the Potouqing Fault further confirm that gold mineralization within and above the Xiejia diorite occurred broadly coevally during the Early Cretaceous, penecontemporaneous with the formation of known gold deposits in the Linglong ore field and other locations in the Jiaodong province at ca. 120 Ma (Yang and Zhou, 2001; Li et al., 2003; Zhang et al., 2020; Deng et al., 2020a). It is noteworthy that the age of gold deposition constrained from geochronological data of ore and gangue minerals is indistinguishable from U-Pb ages of magmatic titanite and zircon grains from the Xiejia diorite (Fig. 14). This consistency suggests a likely genetic relationship between the gold mineralization and deep-seated magmatism represented by the Xiejia diorite (further discussed below).

Genesis of gold mineralization in the diorite

Sulfur and Pb isotope data presented here provide useful information on the origin of the gold mineralization in the Xiejia diorite. Because pyrite is the predominant sulfur-bearing mineral in the mineralized diorite, it is reasonable to assume that the pyrite $\delta^{34}S_{CDT}$ values represent the bulk sulfur isotopic composition of the ore fluids (Ohmoto and Rye, 1979). Gold-bearing pyrite grains from the diorite have $\delta^{34}S_{CDT}$ values ranging from 2.1 to 9.7 ‰ with an average of 5.3‰ (Supplemental Table S11), which overlap the sulfur isotopic compositions of the Early Cretaceous intermediate-mafic dikes in the Jiaodong province ($\delta^{34}S_{CDT}$ = 0.8 to 10.8 ‰; Huang, 1994; Zhang et al., 2014). These values are slightly to moderately higher than those typical of magmatic sulfur, likely reflecting: (1) derivation from an oxidized magma (Deng et al., 2020b; Zhu et al., 2015), which is partly supported by the presence of abundant magnetite, high ferric iron contents, and positive Ce anomaly of magmatic titanite in the Xiejia diorite (Supplemental Table S9, Fig. 12; King et al., 2013), (2) partial melting of a metasedimentary lower crustal source as partly supported by the abundant inherited zircon with a broad spread of ages, and/or (3) mixing with meteoric water which had leached heavy S isotope from the Jiaodong Group (e.g., Yuan et al., 2019). The $\delta^{34}S_{CDT}$ values of pyrite from the alteration zone along the Potouqing Fault vary from 5.8 to 8.1 ‰ (Supplemental Table S11, Fig. 13B), which overlap values of gold deposits in the Linglong ore field (6.4 to 8.6 ‰) (Hou et al., 2006) and are consistent with those from the mineralized Xiejia diorite (Fig. 13B). Thus, the sulfur isotope data suggest a common magmatic sulfur source for gold mineralization both in the Xiejia diorite and in the Linglong ore field.

Pyrite from the Xiejia diorite has Pb isotope ratios (Supplemental Table S12) consistent with those of pyrite from the mineralized alteration zone of the Potouqing Fault and partly overlapping the coeval mafic dikes in the Linglong ore field (Fig. 13C-D). This observation suggests a similar magmatic lead source. There is a linear trend of Pb isotopes from plagioclase and pyrite in the diorite to pyrite in the alteration assemblages in the Potouqing Fault and the gold deposits in the Linglong ore field (Fig. 13C-D), suggesting that progressive partial alteration of plagioclase in the intrusion could have played a key role in fractionation of the Pb isotopes. Collectively, the S and Pb isotope data indicate a magmatic origin for the gold mineralization in the diorite. This view is confirmed by the age similarity between gold mineralization and the Xiejia diorite.

The close spatial and temporal relationships and similar isotopic compositions between the diorite and the alteration zone along the Potouqing Fault (Fig. 2B) suggest two possible scenarios for the origin of the disseminated gold mineralization in the diorite: (1) deep-seated magmatic hydrothermal fluids ascended along the Potouqing Fault and then altered the pre-existing Xiejia diorite, or (2) hydrothermal fluid originating from the Xiejia diorite and/or an underlying magma chamber gradually altered and mineralized the upper part of the intrusion, and subsequent migration of this fluid along the Potouqing Fault caused extensive alteration and gold mineralization.

The first scenario can be excluded because the alteration minerals show a progressive decrease in temperature from the intrusion to the above fault zone, consistent with the cooling of an intrusion-derived fluid as it altered the wall rocks. Alteration assemblages in the diorite, including hydrothermal titanite with temperatures mostly above 300℃ (e.g., Browne, 1978, Cao et al., 2015), attest to higher fluid temperatures in the most altered part of the diorite. In contrast, alteration assemblages along the Potouqing Fault have relatively low-temperature hydrothermal mineral assemblages that mainly formed below 300℃ (Yang et al., 2016).

Thus, we favor the second model, in which gold mineralization formed from hydrothermal fluids exsolved from the Xiejia diorite and/or underlying magma chamber, which was the feeder of the Xiejia diorite. This conclusion is supported by several lines of evidence: (1) miarolitic cavities in the diorite are commonly filled with hydrothermal minerals such as coarse-grained calcite (Figs. 3A-B, 4D). Such cavities are generally considered to reflect abundant volatiles during the late stages of magma evolution (Candela, 1997). (2) Gold mineralization accompanied by hydrothermal alteration occurs both in the diorite and the overlying Potouqing Fault (Figs. 2, 3). The close tempo-spatial relationships between mineralization in the diorite and the Potouqing Fault and the similar S-Pb isotopic signatures suggest a common fluid source.

Petrogenesis of the gold-mineralized diorite

The Xiejia diorite is geochemically and isotopically consistent with the Early Cretaceous mafic to intermediate dikes that are widely distributed in the Linglong ore field (Fig. 2A) and throughout the Jiaodong province. These dikes consistently display arc-like trace element patterns and Sr-Nd-Pb isotopic compositions, and are thought to have been derived from an enriched lithospheric mantle source (Liu et al., 2009; Cai et al., 2015; Long et al., 2017; Wang et al., 2020a). The emplacement age and geochemical signatures of the Xiejia diorite are comparable to those of the mafic to intermediate dikes (Figs, 10, 11, 14), permitting the inference that the Xiejia diorite was most likely derived from the same source.

The Xiejia diorite contains Archean to Late Jurassic inherited zircons (Supplemental Table S2, Fig. 7). The presence of Neoproterozoic zircons in the Xiejia diorite likely reflects deep subduction of the Yangtze craton beneath the NCC or insertion of rocks of the Yangtze craton into the nearby crust of the NCC by thrusting and folding (Zhai, 2010). This interpretation is supported by the general absence of Neoproterozoic rocks in the NCC and their abundance in the Yangtze craton (Zheng et al., 2004). However, the Xiejia diorite cannot be explained simply by significant contamination of mafic magmas by crustal materials. Such a process would have led to significant increases in the initial $^{87}Sr/^{86}Sr$ ratios of the diorite and a progressive decrease in $\varepsilon_{Nd}(t)$ values with increasing SiO_2 (Ma et al., 2014a). Instead, the Xiejia diorite is characterized by relatively constant Sr-Nd isotopes that do not vary with changes of SiO_2 but are consistent with those of coeval mafic dikes in the Jiaodong province (Fig. 11E-F). Such homogeneous Sr-Nd isotopes suggest that the assimilation of crustal materials from the Yangtze craton was too subtle to affect the isotope signature of the diorite magma. In addition, the diorite has much higher Sr (844-1220 ppm), Rb (63.5-126.5 ppm), and Ba (1090-1945 ppm) contents than those of crustal rocks from the NCC and Yangtze craton (Sr = 254-350 ppm; Rb = 59-79 ppm; Ba = 633-688 ppm) (Gao et al., 1998). Thus, the enriched Sr-Nd isotopes and negative Nb-Ta-Ti-Zr-Hf anomalies of the Xiejia diorite represent original features of the metasomatized mantle source rather than having been caused by crustal contamination (Thirlwall et al., 1994).

Other geochemical characteristics of the Xiejia diorite, such as LILE enrichment and HFSE depletion, are similar to those of Aleutian arc basalts derived from partial melting of a mantle peridotite metasomatized by slab fluids (Kelemen et al., 2014). However, the Xiejia diorite has much higher initial $^{87}Sr/^{86}Sr$ ratios than normal slab fluids ($^{87}Sr/^{86}Sr$ = 0.7041; Tatsumi, 2001). Aqueous fluids from the altered oceanic crust ($^{87}Sr/^{86}Sr$ = 0.7092; Tatsumi, 2001) and/or marine sediments ($^{87}Sr/^{86}Sr$ = 0.7053-0.7312; Plank and Langmuir, 1998) are the most likely source of the high initial Sr isotopic ratios of the Xiejia diorite. The oceanic crust has higher $\varepsilon_{Nd}(t)$ and $\varepsilon_{Hf}(t)$ values (e.g., MORB > 0; Hofmann, 2004) than those of the Xiejia diorite (Fig. 11A-B), which means that a metasomatic agent derived merely from subducted oceanic crust cannot explain the low $\varepsilon_{Nd}(t)$ and $\varepsilon_{Hf}(t)$ values of the Xiejia diorite. Chemical modeling of Tatsumi and Hanyu (2003) showed that only a small amount of sediment-derived fluid (<0.1%) would suffice to modify the isotopic signature of subduction-related magmas. Thus, fluids released from subducted marine sediments may have played an important role in metasomatizing the mantle source of the Xiejia diorite magma. Recent studies have proposed that subduction of the Yangtze Craton beneath the NCC may also have led to metasomatization of the sub-continental lithospheric mantle (SCLM) beneath the Jiaodong province (Wang et al., 2020a; Xiong et al., 2020, 2021).

In summary, the Xiejia diorite was most likely derived from an enriched lithospheric mantle source that was modified by melt/fluid liberated from a subducting oceanic slab containing marine sediments and/or continental crust associated with subduction of the Yangtze Craton beneath the NCC. In addition to the Xiejia diorite, many other coeval mafic rocks including lamprophyres, gabbros, and basalts occur in the Jiaodong province, all of which were most likely derived from a similar enriched lithospheric mantle source (Xu et al., 2004; Yang et al., 2004; Gao et al., 2008; Wang et al., 2020a; Koua et al., 2022). The presence of these magmatic rocks, together with coeval faulted basin and metamorphic core complexes in the eastern NCC are regarded as shallow responses to the destruction of the NCC during the Late Mesozoic (Zhu et al., 2012, 2015; Wu et al., 2019).

Implications for the origin of decratonization-related gold deposits

Numerous geochronological studies have shown that gold mineralization in the Jiaodong district occurred at ca. 120 Ma (Yang and Zhou, 2001; Li et al., 2003, 2006; Yuan et al., 2019; Zhang et al., 2020), coincident with the peak of destruction of the NCC (Zhu et al., 2011, 2012). Accordingly, these gold deposits have been defined as decratonization-related gold deposits, and their genesis has been interpreted to be related to mantle-derived magmatism in an extensional setting associated with lithospheric destruction (Li et al., 2003; Zhu et al., 2012, 2015). Some previous researchers proposed that the mineralizing fluids were derived directly from the subducting Paleo-Pacific slab or dehydrating metasomatized mantle (Goldfarb and Santosh, 2014; Groves and Santosh, 2016; Groves et al., 2020). In either model, it is uncertain how gold was extracted from the mantle and finally deposited in the upper crust at Jiaodong.

The results presented here indicate that the gold in the Xiejia diorite and the Linglong ore field was deposited from magmatic hydrothermal fluids exsolved from the diorite magma and/or a deeper-seated magma chamber (Fig. 15). The Xiejia diorite and coeval mafic dikes were both derived from parental magmas generated from the enriched lithospheric mantle, which was extensively modified by slab-derived melts/fluids prior to destruction of the NCC (Ma et al., 2014b; Deng et al., 2017; Wang et al., 2020a). Gold may have been preferentially extracted by volatile-rich, shoshonitic, mafic magmas from the metasomatized mantle source (Wang et al., 2020b; Wang et al., 2022), comparable to the metal enrichment seen in alkali basalts in partially melted xenoliths of metasomatised mantle (Rielli et al., 2022). Minor amounts of such magmas rose rapidly due to their low viscosity and were emplaced into shallow fractures to form the extensive mafic dikes (best represented by lamprophyres) as a prelude to the gold mineralization. With extensive thinning of the NCC and associated melting of the lithospheric mantle, large volumes of mafic magma accumulated in the lower crust where it evolved through assimilation and fractional crystallization (AFC). If gold and sulfides were present in the lower crustal materials, it is possible that the mantle-derived magmas were further enriched during the AFC processes (e.g., Tomkins and Mavrogenes, 2003). The remaining magma then migrated upward and was emplaced into the overlying fault system in the shallow crust as represented by the Xiejia diorite intrusion. Auriferous fluids exsolved from the cooling magma altered the upper part of the diorite leading to the disseminated gold mineralization. Further migration of the fluids along the Potouqing Fault and its subsidiary structures caused extensive alteration and gold mineralization at Dongfeng. By inference, other gold vein deposits in the Linglong ore field may have also formed by a similar process.

Destruction of the NCC in the Early Cretaceous, accompanied by lithospheric thinning and extensional tectonism, caused significantly elevated heat flow and produced voluminous mafic magmas from the SCLM (Wu et al., 2005; Zhu et al., 2012, 2020; this study). In this setting, the mantle and lower crust underlying the Jiaodong gold province were too hot for fluids to pass through without causing melting (Tomkins and Grundy, 2009; Weinberg and Hasalová, 2015; Phillips, 2022). Thus, it is highly improbable that fluids generated from a subducting slab or metasomatized mantle beneath Jiaodong were able to migrate directly to the sites of ore formation in the upper crust (e.g., Goldfarb and Santosh, 2014; Groves and

Santosh, 2016). Our study therefore not only confirms that the giant Jiaodong gold province originated from mantle-derived magmas, but also supports the incorporation of gold and sulfur into the hydrothermal fluids exsolved from an upper crustal magma chamber. This model addresses most of the controversies discussed in recent literature and emphasizes the key role of both metasomatized mantle and tectonic evolution in the formation of decratonization-related gold deposits. Moreover, the gold metallogenic model from the Jiaodong province may have important implications on the source and process of other gold systems, which are hosted in ancient cratons that have undergone destruction or deformation like the NCC, e.g., Nevada's Carlin-type gold deposits in the western North America Craton (Cline et al., 2005; Muntean et al., 2011).

CONCLUSIONS

Our results provide strong evidence that mantle-derived magmatism played an important role in the formation of the giant gold deposits of the Jiaodong province. The main conclusions are summarized as follows:

(1) Results of zircon LA-ICP-MS U-Pb, titanite LA-ICP-MS U-Pb, pyrite ID-NTIMS Re-Os, and sericite $^{40}Ar/^{39}Ar$ dating consistently indicate that disseminated gold mineralization in the Xiejia diorite occurred at ca. 120 Ma, coevally with emplacement of the intrusion and gold mineralization in the Linglong ore field.

(2) Gold-bearing pyrite grains from the Xiejia diorite have $\delta^{34}S_{CDT}$ values and Pb isotopic ratios that are consistent with those of the contemporaneous mafic dikes in the Linglong ore field, suggesting a magmatic source for the gold. The ore fluids were derived from the diorite magma and/or a deeper magma chamber beneath the diorite.

(3) The Xiejia diorite is shoshonitic and metaluminous in composition and is characterized by LILE and LREE enrichment and HFSE depletion. In addition, it has negative Nb, Ta, and Ti anomalies, high initial $^{87}Sr/^{86}Sr$ ratios, low $\varepsilon_{Nd}(t)$ and $\varepsilon_{Hf}(t)$ values, and low Pb isotopic ratios. These geochemical signatures are similar to those of the mafic dikes closely associated with gold veins in the Jiaodong province, suggesting that both originated from an enriched lithospheric mantle source.

(4) Mafic magmas, which were generated by partial melting of the enriched lithospheric mantle beneath the NCC due to its thinning and destruction in the Early Cretaceous, extracted gold, sulfur, and other volatiles from the source region. The parental magmas not only produced extensive mafic magmatism in the Jiaodong district, but also accumulated in the lower crust where they were modified by MASH processes, and then migrated to a magma chamber in the upper crust. Auriferous hydrothermal fluids exsolved from the cooling magma, leading to the deposition of gold and sulfide minerals in shallow fractures associated with regional faults, finally forming the giant gold deposits in the Jiaodong province.

ACKNOWLEDGMENTS

We thank Yuquan Yang from the Shandong Zhaojin Group Co. LTD and Hui Yang and Xiling Luo from China University of Geosciences (Wuhan) for their assistance with the field studies at Jiaodong. We are indebted to Huaning Qiu, Kuidong Zhao, Chris Ottley, Geoff Nowell, and Keqing Zong for supporting laboratory work and Paul Dirks, Biji Luo, Hao Hu, Xiaoye Jin, and Kang Cao for constructive discussions. We also thank Dr. Catherine Mottram (Associate Editor) and two anonymous reviewers for their critical and constructive comments that helped to improve the manuscript. Our thanks are extended to Prof. Brad Singer of the *Geological Society of America Bulletin* for handling this manuscript. This study was jointly supported by the Natural Science Foundation of China (42172103, 42130814, 42273023) and the Ministry of Science and Technology of China (2016YFC0600104).

REFERENCES CITED

Browne, P.R.L, 1978, Hydrothermal Alteration in Active Geothermal Fields: Annual Review of Earth and Planetary Sciences, v. 6 (1), p. 229-248, https://doi.org/10.1146/annurev.ea.06.050178.001305.

Cai, Y., Fan, H., Santosh, M., Hu, F., Yang, K., and Hu, Z., 2015, Subduction-related metasomatism of the lithospheric mantle beneath the southeastern North China Craton: Evidence from mafic to intermediate dykes in the northern Sulu orogen: Tectonophysics, v. 659, p. 137-151, https://doi.org/10.1016/j.tecto.2015.07.037.

Candela, P. A., 1997, A Review of Shallow, Ore-related Granites: Textures, Volatiles, and Ore Metals: Journal of Petrology, v. 38, p. 1619-1633, https://doi.org/10.1093/petroj/38.12.1619.

Cao, M., Qin, K., Li, G., Evans, N.J., and Jin, L., 2015, In situ LA-(MC)-ICP-MS trace element and Nd isotopic compositions and genesis of polygenetic titanite from the Baogutu reduced porphyry Cu deposit, Western Junggar, NW China: Ore Geology Reviews, v. 65, p. 940-954, http://dx.doi.org/10.1016/j.oregeorev.2014.07.014.

Charles, N., Gumiaux, C., Augier, R., Chen, Y., Faure, M., Lin, W., and Zhu, R., 2012, Metamorphic Core Complex dynamics and structural development: Field evidences from the Liaodong Peninsula (China, East Asia): Tectonophysics, v. 560-561, p. 22-50, https://doi.org/10.1016/j.tecto.2012.06.019.

Cline, J.S., Hofstra, A.H., Muntean, J.L., Tosdal, R.M., and Hickey, K.A., 2005, Carlin-Type Gold Deposits in Nevada: Critical Geologic Characteristics and Viable Models. *In*: Hedenquist J W, Thompson J F H, Goldfarb R J, Richards J P, Eds., Economic Geology, 100th Anniversary Volume, p. 451-484.

Cox, K. G., Bell, J. D., and Pankhurst, R. J., 1979, The Interpretation of Igneous Rocks: London, George Allen & Unwin, 450 p.

Deng, J., Yang, L., Sun, Z., Wang, J., Wang, Q., Xin, H., and Li, X., 2003, A Metallogenic Model of Gold Deposits of the Jiaodong Granite-Greenstone Belt: Acta Geological Sinica-English Edition, v. 77, p. 537-546, https://doi.org/10.1111/j.1755-6724.2003.tb00134.x.

Deng, J., Wang, C., Bagas, L., Carranza, E. J. M., and Lu, Y., 2015, Cretaceous–Cenozoic tectonic history of the Jiaojia Fault and gold mineralization in the Jiaodong Peninsula, China: constraints from zircon U-Pb, illite K-Ar, and apatite fission track thermochronometry: Mineralium Deposita, v. 50, p.

987-1006, https://doi.org/10.1007/s00126-015-0584-1.

Deng, J., Liu, X., Wang, Q., Dilek, Y., and Liang, Y., 2017, Isotopic characterization and petrogenetic modeling of Early Cretaceous mafic diking–Lithospheric extension in the North China craton, eastern Asia: GSA Bulletin, v. 129, p. 1379-1407, https://doi.org/ 10.1130/B31609.1.

Deng, J., Yang, L., Groves, D. I., Zhang, L., Qiu, K., and Wang, Q., 2020a, An integrated mineral system model for the gold deposits of the giant Jiaodong province, eastern China: Earth-Science Reviews, v. 208, p. 103274, https://doi.org/10.1016/j.earscirev.2020.103274.

Deng, J., Wang, Q., Santosh, M., Liu, X., Liang, Y., Yang, L., Zhao, R., and Yang, L., 2020b, Remobilization of metasomatized mantle lithosphere: a new model for the Jiaodong gold province, eastern China: Mineralium Deposita, v. 55, p. 257-274, https://doi.org/10.1007/s00126-019-00925-0.

Dong, Y., Zhang, G., Neubauer, F., Liu, X., Genser, J., and Hauzenberger, C., 2011, Tectonic evolution of the Qinling orogen, China: Review and synthesis: Journal of Asian Earth sciences, v. 41, p. 213-237, https://doi.org/10.1016/j.jseaes.2011.03.002.

Fan, H. R., Zhai, M. G., Xie, Y. H., and Yang, J. H., 2003, Ore-forming fluids associated with granite-hosted gold mineralization at the Sanshandao deposit, Jiaodong gold province, China: Mineralium Deposita, v. 38, p. 739-750, https://doi.org/10.1007/s00126-003-0368-x.

Gao, S., Luo, T., Zhang, B., Zhang, H., Han, Y., Zhao, Z., and Hu, Y., 1998, Chemical composition of the continental crust as revealed by studies in East China: Geochimica et Cosmochimica Acta, v. 62, p. 1959-1975, https://doi.org/10.1016/S0016-7037(98)00121-5.

Gao, S., Rudnick, R. L., Xu, W. L., Yuan, H. L., Liu, Y. S., Walker, R. J., Puchtel, I. S., Liu, X., Huang, H., and Wang, X. R., 2008, Recycling deep cratonic lithosphere and generation of intraplate magmatism in the North China Craton: Earth and Planetary Science Letters, v. 270, p. 41-53, https://doi.org/ 10.1016/j.epsl.2008.03.008.

Goldfarb, R. J., and Santosh, M., 2014, The dilemma of the Jiaodong gold deposits: Are they unique? Geoscience Frontiers, v. 5, p. 139-153, https://doi.org/ 10.1016/j.gsf.2013.11.001.

Goss, S. C., Wilde, S. A., Wu, F., and Yang, J., 2010, The age, isotopic signature and significance of the youngest Mesozoic granitoids in the Jiaodong Terrane, Shandong Province, North China Craton: Lithos, v. 120, p. 309-326, https://doi.org/ 10.1016/j.lithos.2010.08.019.

Groves, D. I., and Santosh, M., 2016, The giant Jiaodong gold province: The key to a unified model for orogenic gold deposits? Geoscience Frontiers, v. 7, p. 409-417, https://doi.org/ 10.1016/j.gsf.2015.08.002.

Groves, D. I., Santosh, M., Deng, J., Wang, Q., Yang, L., and Zhang, L., 2020, A holistic model for the origin of orogenic gold deposits and its implications for exploration: Mineralium Deposita, v. 55, p. 275-292, https://doi.org/ 10.1007/s00126-019-00877-5.

Hart, S. R., 1984, A large-scale isotope anomaly in the Southern Hemisphere mantle: Nature, v. 309, p. 753-757, https://doi.org/10.1038/309753a0.

Hofmann, A. W., 2004, Sampling mantle heterogeneity trough oceanic basalts: isotopes and trace elements, *in* R.W. Carlson Ed., Treatise on Geochemistry, v. 2, p. 61-101.

Hoskin, P., and Schaltegger, U., 2003, The Composition of Zircon and Igneous and Metamorphic

Petrogenesis: Reviews in Mineralogy and Geochemistry, v. 53, p. 27-62.

Hou, M. L., Jiang, S. Y., Jiang, Y. H., and Ling, H. F., 2006, S-Pb isotope geochemistry and Rb-Sr geochronology of the Penglai gold field in the eastern Shangdong province: Acta Petrologica Sinica, v. 22, p. 2525-2533 (in Chinese with English abstract), https://doi.org/10.3321/j.issn:1000-0569.2006.10.013.

Hou, M. L., Jiang, Y. H., Jiang, S. Y., Ling, H. F., and Zhao, K. D., 2007, Contrasting origins of late Mesozoic adakitic granitoids from the northwestern Jiaodong Peninsula, east China: implications for crustal thickening to delamination: Geological Magazine, v. 144, p. 619-631, https://doi.org/10.1017/S0016756807003494.

Huang, D. Y., 1994, Sulfur Isotope Studies of the Metallogenic Series of Gold Deposits in Jiaodong (Eastern Shandong) Area: Mineral Deposits, v. 13, p. 75-87 (in Chinese with English Abstract).

Jahn, B. M., Wu, F. Y., Lo, C. H., Tsai, C. H., 1999, Crust-mantle interaction induced by deep subduction of the continental crust: Geochemical and Sr-Nd isotopic evidence from post-collisional mafic-ultramafic intrusions of the northern Dabie complex, central China: Chemical Geology, v. 157, p. 119-146, https://doi.org/10.1016/S0009-2541(98)00197-1.

Jahn, B., Liu, D., Wan, Y., Song, B., and Wu, J., 2008, Archean crustal evolution of the Jiaodong Peninsula, China, as revealed by zircon SHRIMP geochronology, elemental and Nd-isotope geochemistry: American Journal of Science, v. 308, p. 232-269, https://doi.org/10.2475/03.2008.03.

Kelemen, P. B., Hanghøj, K., and Greene, A. R., 2014, One View of the Geochemistry of Subduction-Related Magmatic Arcs, with an Emphasis on Primitive Andesite and Lower Crust, *in* Holland, H. D., and Turekian, K. K., eds., Treatise on Geochemistry (Second Edition): Oxford, Elsevier, p. 749-806.

King, P. L., Sham, T. K., Gordon, R. A., and Dyar M.D., 2013, Microbeam x-ray analysis of ce^{3+}/ce^{4+} in Ti-rich minerals: a case study with titanite (sphene) with implications for multivalent trace element substitution in minerals: American Mineralogist, v. 98, p. 110-119, https://doi.org/10.2138/am.2013.3959.

Koua, K., Sun, H., Li, J., Li, H., Xie, J., Sun, Q., Li, Z., Yang, H., Zhang, L., and Mondah, O. R., 2022. Petrogenesis of Early Cretaceous granitoids and mafic enclaves from the Jiaodong Peninsula, eastern China: implications for crust-mantle interaction, tectonic evolution and gold mineralization, Journal of Asian Earth Sciences, v. 228, p. 105096, https://doi.org/10.1016/j.jseaes.2022.105096.

Kuang, Y., Pang, C., Luo, Z., Hong, L., Zhong, Y., Qiu, H., and Xu, Y., 2012, ^{40}Ar-^{39}Ar geochronology and geochemistry of mafic rocks from Qingshan Group, Jiaodong area: Implications for the destruction of the North China: Acta Petrologica Sinica, v. 28, p. 1073-1091 (in Chinese with English Abstract).

Li, J.W., Vasconcelos, P., Zhang, J., Zhou, M., Zhang, X., and Yang, F., 2003, ^{40}Ar/^{39}Ar Constraints on a Temporal Link between Gold Mineralization, Magmatism, and Continental Margin Transtension in the Jiaodong Gold Province, Eastern China: Journal of Geology, v. 111, p. 741-751, https://doi.org/10.1086/378486.

Li, J.W., Vasconcelos, P., Zhou, M., Zhao, X., and Ma, C., 2006, Geochronology of the Pengjiakuang and

Rushan gold deposits, eastern Jiaodong gold province, northeastern China; implications for regional mineralization and geodynamic setting: Economic Geology, v. 101, p. 1023-1038, https://doi.org/10.2113/gsecongeo.101.5.1023.

Li, J.W., Bi, S.J., Selby, D., Chen, L., Vasconcelos, P., Thiede, D., Zhou, M.F., Zhao, X.F., Li, Z.K., and Qiu, H.N., 2012, Giant Mesozoic gold provinces related to the destruction of the North China craton: Earth and Planetary Science Letters, v. 349-350, p. 26-37, https://doi.org/10.1016/j.epsl.2012.06.058.

Li, Y., and Vermeesch, P., 2021, Short communication: Inverse isochron regression for Re-Os, K-Ca and other chronometers: Geochronology, v. 3, p. 415-420, https://doi.org/10.5194/gchron-2021-7.

Ling, W. L., Duan, R. C., Xie, X. J., Zhang, Y. Q., Zhang, J. B., Cheng, J. P., Liu, X. M., and Yang, H. M., 2009, Contrasting geochemistry of the Cretaceous volcanic suites in Shandong province and its implications for the Mesozoic lower crust delamination in the eastern North China craton: Lithos, v. 113, p. 640-658, https://doi.org/10.1016/j.lithos.2009.07.001.

Liu, D. Y., Nutman, A. P., Compston, W., Wu, J. S., and Shen, Q. H., 1992, Remnants of ≥3800 Ma crust in the Chinese part of the Sino-Korean Craton: Geology, v. 20, p. 339-342, https://doi.org/10.1130/0091-7613(1992)020<0339:ROMCIT>2.3.CO;2.

Liu, G., Song, G., Bao, Z., Li, R., Wen, G., Liu, J., and Liu C., Guo Z., Fan J., Yan C., and Li S., 2019, New Breakthrough of Deep Prospecting in the Northern Section of the Zhaoping Fault Zone and the New Understanding of Fault Distribution in the Jiaodong District: Geotectonica et Metallogenia, v. 43, p. 226-234 (in Chinese with English Abstract).

Liu, S., Hu, R., Gao, S., Feng, C., Yu, B., Feng, G., Qi, Y., Wang, T., and Coulson, I. M., 2009, Petrogenesis of Late Mesozoic mafic dykes in the Jiaodong Peninsula, eastern North China Craton and implications for the foundering of lower crust: Lithos, v. 113, p. 621-639, https://doi.org/10.1016/j.lithos.2009.06.035.

Liu, Y., Deng, J., Wang, Z. L., Zhang, L., Zhang, C., Liu, X. D., Zheng, X. L., Wang, X. D., 2014, Zircon U-Pb age, Lu-Hf isotopes and petrogeochemistry of the monzogranites from Xincheng gold deposit, northwestern Jiaodong Peninsula, China: Acta Petrologica Sinica, v. 30, p. 2559-2573 (in Chinese with English abstract).

Long, Q., Hu, R., Yang, Y., Yang, C., Zhou, S., Siebel, W., and Chen, F., 2017, Geochemistry of Early Cretaceous Intermediate to Mafic Dikes in the Jiaodong Peninsula: Constraints on Mantle Source Composition beneath Eastern China: The Journal of Geology, v. 125, p. 713-732.

Ma, L., Jiang, S., Hou, M., Dai, B., Jiang, Y., Yang, T., Zhao, K., Pu, W., Zhu, Z., and Xu, B., 2014a, Geochemistry of Early Cretaceous calc-alkaline lamprophyres in the Jiaodong Peninsula: Implication for lithospheric evolution of the eastern North China Craton: Gondwana Research, v. 25, p. 859-872, https://doi.org/10.1016/j.gr.2013.05.012.

Ma, L., Jiang, S., Hofmann, A. W., Dai, B., Hou, M., Zhao, K., Chen, L., Li, J., and Jiang, Y., 2014b, Lithospheric and asthenospheric sources of lamprophyres in the Jiaodong Peninsula: A consequence of rapid lithospheric thinning beneath the North China Craton? Geochimica et Cosmochimica Acta, v. 124, p. 250-271, https://doi.org/10.1016/j.gca.2013.09.035.

Ma, L., Jiang, S., Hofmann, A. W., Xu, Y., Dai, B., and Hou, M., 2016, Rapid lithospheric thinning of the

North China Craton: New evidence from cretaceous mafic dikes in the Jiaodong Peninsula: Chemical Geology, v. 432, p. 1-15, https://doi.org/10.1016/j.chemgeo.2016.03.027.

Mao, J., Wang, Y., Li, H., Pirajno, F., Zhang, C., and Wang, R., 2008, The relationship of mantle-derived fluids to gold metallogenesis in the Jiaodong Peninsula: Evidence from D–O–C–S isotope systematics: Ore Geology Reviews, v. 33, p. 361-381, https://doi.org/10.1016/j.oregeorev.2007.01.003.

Muntean, J.L., Cline, J.S., Simon, A.C., and Longo, A.A., 2011, Magmatic-hydrothermal origin of Nevada's Carlin-type gold deposits: Nature Geoscience, v. 4(2), p. 122-127, https://doi.org/10.1038/NGEO1064.

Ohmoto, H., and Rye, R. O., 1979, Isotopes of sulfur and carbon. *In:* Barnes, H.L., Ed., Geochemistry of Hydrothermal Ore Deposits (Second Edition): New York, Wiley-Interscience, 509-567 p.

Peccerillo, A., and Taylor, S. R., 1976, Geochemistry of Eocene Calc-Alkaline Volcanic Rocks from the Kastamonu Area, Northern Turkey: Contributions to Mineralogy and Petrology, v. 58, p. 63-81, https://doi.org/10.1007/BF00384745.

Phillips, N., 2022, Formation of gold deposits. *In*: Dilek, Y., Pirajno, F., and Windley, B., Eds., Modern Approaches in Solid Earth Sciences: Singapore, Springer Nature, v. 21, 291 p.

Plank, T., and Langmuir, C. H., 1998, The chemical composition of subducting sediment and its consequences for the crust and mantle: Chemical Geology, v. 145, p. 325-394, https://doi.org/10.1016/s0009-2541(97)00150-2.

Qiu, Z., Li, Z., and Yuan, Z., 2022, Microstructure and Trace Elements of Pyrite from Sanshandao Gold Deposit in Jiaodong District: Implications for Mechanism of Gold Enrichment: Earth Science, v. 47, p. 290-308, https://doi.org/10.3799/dqkx.2021.045 (in Chinese with English abstract).

Ren, J., Tamaki, K., Li, S., and Junxia, Z., 2002, Late Mesozoic and Cenozoic rifting and its dynamic setting in Eastern China and adjacent areas: Tectonophysics, v. 344, p. 175-205, https://doi.org/10.1016/S0040-1951(01)00271-2.

Rielli, A., Tomkins, A.G., Nebel, O., Brugger, J., Etschmann, B., Evans, K.A., Wykes, J.L., Vasilyev, P., and Paterson, D., 2022, Incipient metal and sulfur extraction during melting of metasomatised mantle: Earth and Planetary Science Letters, v. 599, p. 117850, https://doi.org/10.1016/j.epsl.2022.117850.

SBGMR (Shandong Bureau of Geology and Mineral Resources), 1991, Geology of Shandong province: Beijing, Geological Publishing House, 251 p (in Chinese).

Shandong Zhaojin Group Co. LTD, 2015, Detailed survey report of gold deposit in the Luangjiahe area at Zhaoyuan, Shandong Province, 122 p (in Chinese).

Shen, Y. K., Guo, T., Yang, Y. Q., Chen, Z. L. Wei, C. S., and Sun, H. S., 2016. Discovery of biotite monzonite and Ar-Ar thermochronology significance in Linglong gold field: Journal of Geomechanics, v. 22, p. 778-793 (in Chinese with English abstract).

Tan, J., Wei, J., Audétat, A., and Pettke, T., 2012, Source of metals in the Guocheng gold deposit, Jiaodong Peninsula, North China Craton: Link to early Cretaceous mafic magmatism originating from Paleoproterozoic metasomatized lithospheric mantle: Ore Geology Reviews, v. 48, p. 70-87, https://doi.org/10.1016/j.oregeorev.2012.02.008.

Tan, J., Wei, J., He, H., Su, F., Li, Y., Fu, L., Zhao, S., Xiao, G., Zhang, F., Xu, J., Liu, Y., Stuart, F. M., and Zhu, R., 2018, Noble gases in pyrites from the Guocheng-Liaoshang gold belt in the Jiaodong province: Evidence for a mantle source of gold: Chemical Geology, v. 480, p. 105-115, https://doi.org/10.1016/j.chemgeo.2017.09.027.

Tang, J., Zheng, Y., Wu, Y., Gong, B., and Liu, X., 2007, Geochronology and geochemistry of metamorphic rocks in the Jiaobei terrane: Constraints on its tectonic affinity in the Sulu orogen: Precambrian Research, v. 152, p. 48-82, 10.1016/j.precamres.2006.09.001.

Tatsumi, Y., 2001, Geochemical modeling of partial melting of subducting sediments and subsequent melt-mantle interaction: Generation of high-Mg andesites in the Setouchi volcanic belt, southwest Japan: Geology, v. 29, p. 323-326, https://doi.org/10.1130/0091-7613(2001)0292.0.CO;2.

Tatsumi, Y., and Hanyu, T., 2003, Geochemical modeling of dehydration and partial melting of subducting lithosphere: Toward a comprehensive understanding of high-Mg andesite formation in the Setouchi volcanic belt, SW Japan: Geochemistry Geophysics Geosystems, v. 4, p. 9, https://doi.org/10.1029/2003GC000530.

Thirlwall, M. F., Smith, T. E., Graham, A. M., Theodorou, N., Hollings, P., Davidson, J. P., and Arculus, R. J., 1994, High Field Strength Element Anomalies in Arc Lavas: Source or Process? Journal of Petrology, v. 35, p. 819-838, https://doi.org/10.1093/petrology/35.3.819.

Tian, Z., Han, P., and Xu, K., 1992, The Mesozoic-Cenozoic east China rift system: Tectonophysics, v. 208, p. 341-363, https://doi.org/10.1016/0040-1951(92)90354-9.

Tomkins, A.G., and Mavrogenes, J.A., 2003, Generation of metal-rich felsic magmas during crustal anatexis: Geology, p. 31, v. 765-768, https://doi.org/10.1130/G19499.1.

Tomkins, A. G., and Grundy, C., 2009, Upper temperature limits of orogenic gold deposit formation; constraints from the granulite-hosted Griffin's Find Deposit, Yilgarn Craton: Economic geology, v. 104, p. 669-685, https://doi.org/10.2113/gsecongeo.104.5.669.

Wang, L. G., Qiu, Y. M., McNaughton, N. J., Groves, D. I., Luo, Z. K., Huang, J. Z., Miao, L. C., and Liu, Y. K., 1998, Constraints on crustal evolution and gold metallogeny in the Northwestern Jiaodong Peninsula, China, from SHRIMP U-Pb zircon studies of granitoids: Ore Geology Reviews, v. 13, p. 275-291, https://doi.org/10.1016/S0169-1368(97)00022-X.

Wang, X., Wang, Z., Cheng, H., Foley, S., Xiong, L., and Hu, Z., 2020b, Early cretaceous lamprophyre dyke swarms in Jiaodong Peninsula, eastern North China Craton, and implications for mantle metasomatism related to subduction: Lithos, v. 368-369, p. 105593, https://doi.org/10.1016/j.lithos.2020.105593.

Wang, X., Wang, Z., Cheng, H., Zong, K., Wang, C. Y., Ma, L., Cai, Y., Foley, S., and Hu, Z., 2022, Gold endowment of the metasomatized lithospheric mantle for giant gold deposits: Insights from lamprophyre dykes: Geochimica et Cosmochimica Acta, v. 316, p. 21-40, https://doi.org/10.1016/j.gca.2021.10.006.

Wang, Z., Cheng, H., Zong, K., Geng, X., Liu, Y., Yang, J., Wu, F., Becker, H., Foley, S., and Wang, C. Y., 2020a, Metasomatized lithospheric mantle for Mesozoic giant gold deposits in the North China craton: Geology, v. 48, p. 169-173, https://doi.org/10.1130/G46662.1.

Wang, Z., Xu, Z., Cheng, H., Zou, Y., Guo, J., Liu, Y., Yang, J., Zong, K., Xiong, L., and Hu, Z., 2021, Precambrian metamorphic crustal basement cannot provide much gold to form giant gold deposits in the Jiaodong Peninsula, China: Precambrian Research, v. 354, p.106045, https://doi.org/10.1016/j.precamres.2020.106045.

Weinberg, R. F., and Hasalová, P., 2015, Water-fluxed melting of the continental crust: A review: Lithos, v. 212-215, p. 158-188, https://doi.org/10.1016/j.lithos.2014.08.021.

Winchester, J. A., and Floyd, P. A., 1977, Geochemical discrimination of different magma series and their differentiation products using immobile elements: Chemical Geology, v. 20, p. 325-343, https://doi.org/10.1016/0009-2541(77)90057-2.

Wu, F. Y., Lin, J., Wilde, S., Zhang, X., and Yang, J., 2005, Nature and significance of the Early Cretaceous giant igneous event in eastern China: Earth and Planetary Science Letters, v. 233, p. 103-119, https://doi.org/10.1016/j.epsl.2005.02.019.

Wu, F. Y., Yang, J. H., Xu, Y. G., Wilde, S. A., and Walker, R. J., 2019, Destruction of the North China Craton in the Mesozoic: Annual Review of Earth and Planetary Sciences, v. 47, p. 173-195, https://doi.org/10.1146/annurev-earth-053018-060342.

Wu, X., Zhu, G., Yin, H., Su, N., Lu, Y., Zhang, S., and Xie, C., 2020, Origin of low-angle ductile/brittle detachments: Examples from the Cretaceous Linglong metamorphic core complex in eastern China: Tectonics, v. 39, p. e2020TC006132, https://doi.org/10.1029/2020TC006132.

Xiao, W., Windley, B., Hao, J., and Zhai, M., 2003, Accretion Leading to Collision and the Permian Solonker Suture, Inner Mongolia, China: Termination of the Central Asian Orogenic Belt: Tectonics, v. 22. p. 1069, https://doi.org/10.1029/2002TC001484.

Xiao, W., Windley, B., Sun, S., Li, J., Huang, B., Han, C., Yuan, C., Sun, M., and Chen, H., 2015, A tale of amalgamation of three Permo-Triassic collage systems in central Asia: oroclines, sutures, and terminal accretion: Annual Review of Earth and Planetary Sciences, v. 43, p. 477-507, https://doi.org/10.1146/annurev-earth-060614-105254.

Xie, S., Wu, Y., Zhang, Z., Qin, Y., Liu, X., Wang, H., Qin, Z., Liu, Q., and Yang, S., 2012, U–Pb ages and trace elements of detrital zircons from Early Cretaceous sedimentary rocks in the Jiaolai Basin, north margin of the Sulu UHP terrane: Provenances and tectonic implications: Lithos, v. 154, p. 346-360, https://doi.org/10.1016/j.lithos.2012.08.002.

Xiong, L., Zhao, X., Wei, J., Jin, X., Fu, L., and Lin, Z., 2020, Linking Mesozoic lode gold deposits to metal-fertilized lower continental crust in the North China Craton: Evidence from Pb isotope systematics: Chemical Geology, v. 533, p. 119440, https://doi.org/10.1016/j.chemgeo.2019.119440.

Xiong, L., Zhao, X., Zhao, S., Lin, H., Lin, Z., Zhu, Z., Wang, Z., Li, M. Y. H., and Li, J., 2021, Formation of giant gold provinces by subduction-induced reactivation of fossilized, metasomatized continental lithospheric mantle in the North China Craton: Chemical Geology, v. 580, p. 120362, https://doi.org/10.1016/j.chemgeo.2021.120362.

Xu, Y. G., Ma, J. L., Huang, X. L., Iizuka, Y., Chung, S. L., and Wu, W., 2004, Early Cretaceous gabbroic complex from Yinan, Shandong Province: petrogenesis and mantle domains beneath the North China Craton: International Journal of Earth Sciences, v. 93, p. 1025-1041, https://doi.org/10.1007/s00531-004-0430-7.

Xu, Z., Wang, Z., Guo, J.L., Liu, Y., Guo, J., Cheng, H., Chen, K., Wang, X., Zong, K., Zhu, Z., Hu, Z., and Li, H., 2022, Chalcophile elements of the Early Cretaceous Guojialing granodiorites and mafic enclaves, eastern China, and implications for the formation of giant Jiaodong gold deposits: Journal of Asian Earth Sciences, v. 238, p. 105374, https://doi.org/10.1016/j.jseaes.2022.105374.

Yang, J. H., Zhu, M. F., Liu, W., Zhai, M. G., 2003, Geochemistry and petrogenesis of Guojialing granodiorites from the northwestern Jiaodong Peninsula, eastern China: Acta Petrologica Sinica, v. 19, p. 692-700 (in Chinese with English abstract).

Yang, J., Chung, S., Zhai, M., and Zhou, X., 2004, Geochemical and Sr–Nd–Pb isotopic compositions of mafic dikes from the Jiaodong Peninsula, China: evidence for vein-plus-peridotite melting in the lithospheric mantle: Lithos, v. 73, p. 145-160, https://doi.org/10.1016/j.lithos.2003.12.003.

Yang, J., and Zhou, X., 2001, Rb-Sr, Sm-Nd, and Pb isotope systematics of pyrite; implications for the age and genesis of lode gold deposits: Geology, v. 29, p. 711-714, https://doi.org/10.1130/0091-7613(2001)0292.0.CO;2.

Yang, J. H., Xu, L., Sun, J. F., Zeng, Q., Zhao, Y. N., Wang, H., and Zhu, Y. S., 2021, Geodynamics of decratonization and related magmatism and mineralization in the North China Craton: Science China: Earth Sciences, v. 64, p. 1409-1427, https://doi.org/10.1007/s11430-020-9732-6.

Yang, K., Fan, H., Santosh, M., Hu, F., Wilde, S. A., Lan, T., Lu, L., and Liu, Y., 2012a, Reactivation of the Archean lower crust: Implications for zircon geochronology, elemental and Sr–Nd–Hf isotopic geochemistry of late Mesozoic granitoids from northwestern Jiaodong Terrane, the North China Craton: Lithos, v. 146-147, p. 112-127, https://doi.org/10.1016/j.lithos.2012.04.035.

Yang, K., Wang, J., Lin, J., Zheng, J., Yang, G., and Ji, H., 2012b, Petrogeochemical characteristics and genetic significance of the Aishan pluton in the Jiaodong Peninsula: Geology and Exploration, v. 48, p. 0693-0703 (in Chinese with English abstract), https://doi.org/10.1007/s11783-011-0280-z.

Yang, L., Deng, J., Goldfarb, R. J., Zhang, J., Gao, B., and Wang, Z., 2014, $^{40}Ar/^{39}Ar$ geochronological constraints on the formation of the Dayingezhuang gold deposit: New implications for timing and duration of hydrothermal activity in the Jiaodong gold province, China: Gondwana Research, v. 25, p. 1469-1483, https://doi.org/10.1016/j.gr.2013.07.001.

Yang, L., Deng, J., Guo, L., Wang, Z., Li, X., and Li, J., 2016, Origin and evolution of ore fluid, and gold-deposition processes at the giant Taishang gold deposit, Jiaodong Peninsula, eastern China: Ore Geology Reviews, v. 72, p. 585-602, https://doi.org/10.1016/j.oregeorev.2015.08.021.

Yang, Z. H., Cheng, Y., and Wang, H. Z., 1986, The geology of China: New York, Oxford University Press, 306 p.

Yuan, Z., Li, Z., Zhao, X., Sun, H., Qiu, H., and Li, J., 2019, New constraints on the genesis of the giant Dayingezhuang gold (silver) deposit in the Jiaodong district, North China Craton: Ore Geology Reviews, v. 112, p. 103038, https://doi.org/10.1016/j.oregeorev.2019.103038.

Zhai, M. G., 2010, Tectonic evolution and metallogenesis of North China Craton: Mineral Deposits, v. 29, p. 24-46 (in Chinese with English abstract), https://doi.org/10.1360/972010-741.

Zhang, C., Liu, Y., Liu, X., Feng, J., Huang, T., Zhang, Q., and Wang, X., 2014, Characteristics of sulfur isotope geochemistry of the Xincheng gold deposit, Northwest Jiaodong, China: Acta Petrologica

Sinica, v. 30, p. 2495-2506 (in Chinese with English Abstract), https://doi.org/10.1002/bbpc.19300360520.
Zhang, L., Weinberg, R. F., Yang, L., Groves, D. I., Sai, S., Matchan, E., Phillips, D., Kohn, B. P., Miggins, D. P., Liu, Y., and Deng, J., 2020, Mesozoic Orogenic Gold Mineralization in the Jiaodong Peninsula, China: A Focused Event at 120 ± 2 Ma During Cooling of Pregold Granite Intrusions: Economic Geology, v. 115, p. 415-441, https://doi.org/10.5382/econgeo.4716.
Zhao, G., Wilde, S. A., Cawood, P. A., and Sun, M., 2001, Archean blocks and their boundaries in the North China Craton: lithological, geochemical, structural and P-T path constraints and tectonic evolution: Precambrian Research, v. 107, p. 45-73, https://doi.org/10.1016/S0301-9268(00)00154-6.
Zhao, G., Sun, M., Wilde, S. A., and Sanzhong, L., 2005, Late Archean to Paleoproterozoic evolution of the North China Craton: key issues revisited: Precambrian Research, v. 136, p. 177-202, https://doi.org/10.1016/j.jseaes.2004.06.004.
Zheng, Y., Wu, Y., Chen, F., Gong, B., Li, L., and Zhao, Z., 2004, Zircon U-Pb and oxygen isotope evidence for a large-scale 18O depletion event in igneous rocks during the Neoproterozoic: Geochimica et Cosmochimica Acta, v. 68, p. 4145-4165, https://doi.org/10.1016/j.gca.2004.01.007.
Zhou, J., Wilde, S., Zhao, G., Zheng, C., Jin, W., Zhang, X., and Cheng, H., 2008, SHRIMP U-Pb zircon dating of the Neoproterozoic Penglai Group and Archean gneisses from the Jiaobei Terrane, North China, and their tectonic implications: Precambrian Research, v. 160, p. 323-340, https://doi.org/10.1016/j.precamres.2007.08.004.
Zhu, G., Niu, M., Xie, C., and Wang, Y., 2010, Sinistral to normal faulting along the Tan-Lu Fault Zone: Evidence for geodynamic switching of the East China continental margin: The Journal of Geology, v. 118, p. 277-293, https://doi.org/10.1086/651540.
Zhu, R. X., Chen, L., Wu, F. Y., and Liu, J. L., 2011, Timing, scale and mechanism of the destruction of the North China Craton: Science China: Earth Sciences, v. 41, p. 583-592, https://doi.org/10.1007/s11430-011-4203-4.
Zhu, R. X., Xu, Y. G., Zhu, G., Zhang, H. F., Xia, Q. K., and Zheng, T. Y., 2012, Destruction of the North China Craton: Science China: Earth Sciences, v. 55, p. 1565-1587, https://doi.org/10.1007/s11430-012-4516-y.
Zhu, R. X., Fan, H. R., Li, J. W., Meng, Q. R., Li, S. R., and Zeng, Q. D., 2015, Decratonic gold deposits: Science China: Earth Sciences, v. 58, p. 1523-1537, https://doi.org/10.1007/s11430-015-5139-x.
Zhu, R., Zhu, G., and Li, J., 2020, The North China Craton Destruction: Beijing, Science Press, 417 p (in Chinese).
Zhu, R., and Sun, W., 2021, The big mantle wedge and decratonic gold deposits: Science China: Earth Sciences, v. 64, p. 1451-1462, https://doi.org/10.1007/s11430-020-9733-1.

FIGURE CAPTIONS

Fig. 1 Geological map of the Jiaodong province showing the distribution of the main Au deposits in this district (modified from Li et al., 2003; Yang et al., 2014). Also shown in the insert map is the location of the Jiaodong gold province in the eastern margin of North China Craton. Abbreviations: TNCO: Trans-North China Orogen, UHP: ultrahigh pressure.

Fig. 2 A. Geological map of the Linglong ore field (modified from Yang et al., 2016; Shandong Zhaojin Group Co. LTD, 2015), showing the distribution of major faults and representative gold deposits, and providing the location of the drill holes (72-ZK1 and 84-ZK1) which intersected the mineralized diorite. B. Cross-section along prospecting line 72 (modified from Shen et al., 2016) and simplified geological column for 72-ZK1 (Supplemental Fig. S1) in the Xiejia area.

Fig. 3 Photographs showing features of the Xiejia diorite (A-C) and the alteration zone along the Potouqing Fault (D) intersected by the drill holes. Locations of the samples are shown in Fig. 2B. A and B. Typical rocks of the Xiejia diorite, which are comprised of amphibole, plagioclase, biotite, and quartz. Note the distribution of disseminated pyrite and calcite. C. Top of the Xiejia diorite. Note the appearance of hydrothermal minerals including epidote and pyrite. D. Silicification and sericitization in the Potouqing Fault zone. Note the common presence of sulfide minerals including pyrite, sphalerite, and galena in all the samples. Abbreviations: Am = amphibole, Bt = biotite, Pl = plagioclase, Kfs = K-feldspar, Ep = epidote, Qtz = quartz, Py = pyrite, Sp = sphalerite, Gn = galena, Ser = sericite, Cal = calcite.

Fig. 4 Photomicrographs under crossed polarized light (CPL) showing minerals and textures of the Xiejia diorite. A. Fresh rock showing the dominant compositions of the diorite: plagioclase, biotite, amphibole. B. Amphibole and plagioclase of the diorite replaced by chlorite and sericite, respectively. C. Core of a plagioclase grain replaced by sericite and calcite. Note the large pyrite grain. D. Coarse-grained epidote and calcite in the diorite. Abbreviations: Chl = chlorite, others as in Fig. 3.

Fig. 5 Photomicrographs under transmitted light (A), reflected light (C, E) and corresponding BSE images (B, D, F) showing the characteristics of different types of titanite in the Xiejia diorite. A, B. Magmatic titanite (Ttn-M) coexisting with amphibole, plagioclase, and biotite from a fresh diorite rock. The titanite is euhedral to subhedral, showing a core-rim texture in the BSE image (B). C, D. Hydrothermal titanite of type 1 (Ttn-H1) intergrown with pyrite and quartz from an altered sample of diorite. The titanite is irregular with a patchy texture in the BSE image (B). E, F. Hydrothermal titanite of type 2 (Ttn-H2) displaying a typical replacement texture and coexisting with chlorite and calcite. Note the rutile and bastnaesite that occur in the relict texture of titanite. Abbreviations: Ttn = titanite, Bsn = bastnaesite, Rt = rutile, Others as in Figs. 3-4.

Fig. 6 Photomicrographs showing the characteristics of sulfide and gold minerals in the Xiejia diorite (A-D) and alteration zone of the Potouqing Fault (E-F). A and F are under transmitted light, whereas others are under reflected light. A. Pyrite and chlorite have replaced an amphibole grain. B. Native gold occurs as infillings of microfractures in pyrite, and as micro-inclusions hosted in quartz. Note that titanite is intergrown with pyrite. C. Coexisting pyrite, pyrrhotite, and chalcopyrite. D. Coexisting pyrite and hydrothermal titanite, which are replaced or cut by pyrrhotite. E. Sulfide aggregation including pyrite, sphalerite, chalcopyrite, and galena in the alteration zone. Note that native gold occurs as micro-inclusions in the sphalerite F. Hydrothermal sericite in close association with pyrite in the alteration zone. Abbreviations: Au = native gold, Ccp = chalcopyrite, Po = pyrrhotite, others as in Figs. 3-5.

Fig. 7 LA-ICP-MS U-Pb Concordia diagrams (A, C) and corresponding $^{206}Pb/^{238}U$ weighted mean ages (B, D) for zircons of the Xiejia diorite. LA-ICP-MS U-Pb Tera-Wasserburg diagrams for magmatic (E) and hydrothermal (F) titanite of the Xiejia diorite. [± *] shows the total uncertainty including the systematic uncertainty.

Fig. 8 Re-Os isochron diagram (A) and inverse isochron diagram (B) for pyrite from the mineralized Xiejia diorite. Three of those pyrite samples (LJH48, LJH61-1, and LJH61-2) yield consistent Re-Os isochron (C) and inverse isochron (D) dates.

Fig. 9 A. $^{40}Ar/^{39}Ar$ age spectra of hydrothermal sericite from the alteration zone along the Potouqing Fault. B. $^{40}Ar/^{39}Ar$ normal isochron of the hydrothermal sericite.

Fig. 10 Major and trace-element plots for the rocks of the Xiejia diorite. A. SiO_2 vs. Na_2O + K_2O (after Cox et al., 1979). B. Nb/Y vs. Zr/TiO_2 (after Winchester and Floyd, 1977). C. SiO_2 vs. K_2O (after Peccerillo and Taylor, 1976). D. A/CNK vs. A/NK. E. Chondrite-normalized REE patterns. F. Primitive mantle-normalized immobile trace element patterns. All major element contents were normalized to 100% on a LOI-free basis before plotting in the diagrams. Data for the coeval mafic dikes in the Linglong ore field are shown for comparison in E and F (Yang et al., 2004).

Fig. 11 A. Initial $^{87}Sr/^{86}Sr$ vs. $\varepsilon_{Nd}(t)$ diagram for the Xiejia diorite. B. T vs. $\varepsilon_{Hf}(t)$ diagram for the Xiejia diorite. C, D. $^{206}Pb/^{204}Pb$ vs. $^{208}Pb/^{204}Pb$ and $^{206}Pb/^{204}Pb$ vs. $^{207}Pb/^{204}Pb$ plots for the plagioclase of the Xiejia diorite. E. SiO_2 vs. initial $^{87}Sr/^{86}Sr$ diagram for the Xiejia diorite. F. SiO_2 vs. $\varepsilon_{Nd}(t)$ diagram for the Xiejia diorite. Data sources: Fields for MORB, OIB, and NHRL (north hemisphere reference line) are from Hart (1984). Fields for the lower and upper crust of the NCC are from Jahn et al. (1999). Cretaceous mafic dikes in Jiaodong are from Yang et al. (2004), Liu et al. (2009), Ma et al. (2014a, 2014b), Cai et al. (2015), Deng et al. (2017), and Wang et al. (2020b); Granites in Jiaodong are from Yang et al. (2003), Hou et al. (2007), Yang et al. (2012a), and Liu et al. (2014).

Fig. 12 Major and trace-element plots for magmatic and hydrothermal titanite of the Xiejia diorite. A. $CaO+TiO_2$ vs. $Al_2O_3+Fe_2O_3$. B. Chondrite-normalized REE patterns. C. (La/Yb)N vs. LREE/HREE. D. Eu* vs. Ce*.

Fig. 13 A. Histogram of $\varepsilon_{Nd}(t)$ for the whole-rock diorite and titanite. The $\varepsilon_{Nd}(t)$ data for the mafic dikes from the Linglong ore field are from Yang et al. (2004) and Long et al. (2017). B. Sulfur isotopic histogram for pyrite from the Xiejia diorite and alteration zone along the Potouqing Fault. The S isotopic data of pyrite from a gold deposit in the Linglong ore field are from Hou et al. (2006). C and D. Thorogenic (C) and uranogenic (D) diagrams for the plagioclase and pyrite from the Xiejia diorite and pyrite from the alteration zone along the Potouqing Fault. The Pb isotopic data of pyrite from gold deposits in the Linglong ore field are from Hou et al. (2006).

Fig. 14 Diagram illustrating the ages of magmatism and gold mineralization in the Linglong ore field. Ages of the Xiejia diorite and gold mineralization in/above the diorite are from this study. Ages of the Linglong, Luanjiahe, and Guojialing magmatic rocks and the mafic dikes in the Linglong ore field are from Yang et al. (2004) and Yang et al. (2012a). Ages of gold mineralization in the Linglong ore field are from Yang and Zhou (2001) and Zhang et al. (2020).

Fig. 15 A proposed cartoon illustrating the genesis of the Early Cretaceous mafic magmatism and the process of gold mineralization in the Linglong ore field.

[1]Supplemental Material. Supplemental Material including one text file (analytical methods), three figures, and twelve excel files. Please visit https://doi.org/10.1130/XXXX to access the supplemental material and contact editing@geosociety.org with any questions.

Supplemental Text S1. Analytical methods

Supplemental Figure 1. Geological log showing the detailed rock characters and corresponding gold grade of the drill hole 72ZK1. The gold concentration data is from Shandong Zhaojin Group Co. LTD (2015). Note the anomalous gold grade of diorite deep in the drill hole.

Supplemental Figure 2. CL images of zircon grains with corresponding $^{206}Pb/^{238}U$ dates from the Xiajie diorite.

Supplemental Figure 3. Photomicrographs of representative titanite grains for U-Pb dating from the Xiajie diorite.

Supplemental Table S1. Locations and descriptions of representative samples in this study

Supplemental Table S2. LA-ICP-MS zircon U-Pb data of the Xiejia diorite

Supplemental Table S3. LA-ICP-MS titanite U-Pb data of the Xiejia diorite

Supplemental Table S4. Re-Os isotopic compositions of pyrite from the Xiejia diorite

Supplemental Table S5. $^{40}Ar/^{39}Ar$ isotopic compositions of sericite from the altered zone of the Potouqing Fault

Supplemental Table S6. Major and trace element compositions of the Xiejia diorite

Supplemental Table S7. Sr, Nd, and Hf isotopic compositions of the Xiejia diorite

Supplemental Table S8. In situ Pb isotopic compositions of feldspar from the Xiejia diorite

Supplemental Table S9. Major and trace element compositions of titanite from the Xiejia diorite

Supplemental Table S10. In situ Nd isotopic compositions of titanite from the Xiejia diorite

Supplemental Table S11. In situ S isotopic compositions of pyrite from the Xiejia diorite and alteration zone of the Potouqing Fault

Supplemental Table S12. In situ Pb isotopic compositions of pyrite from the Xiejia diorite and alteration zone of the Potouqing Fault

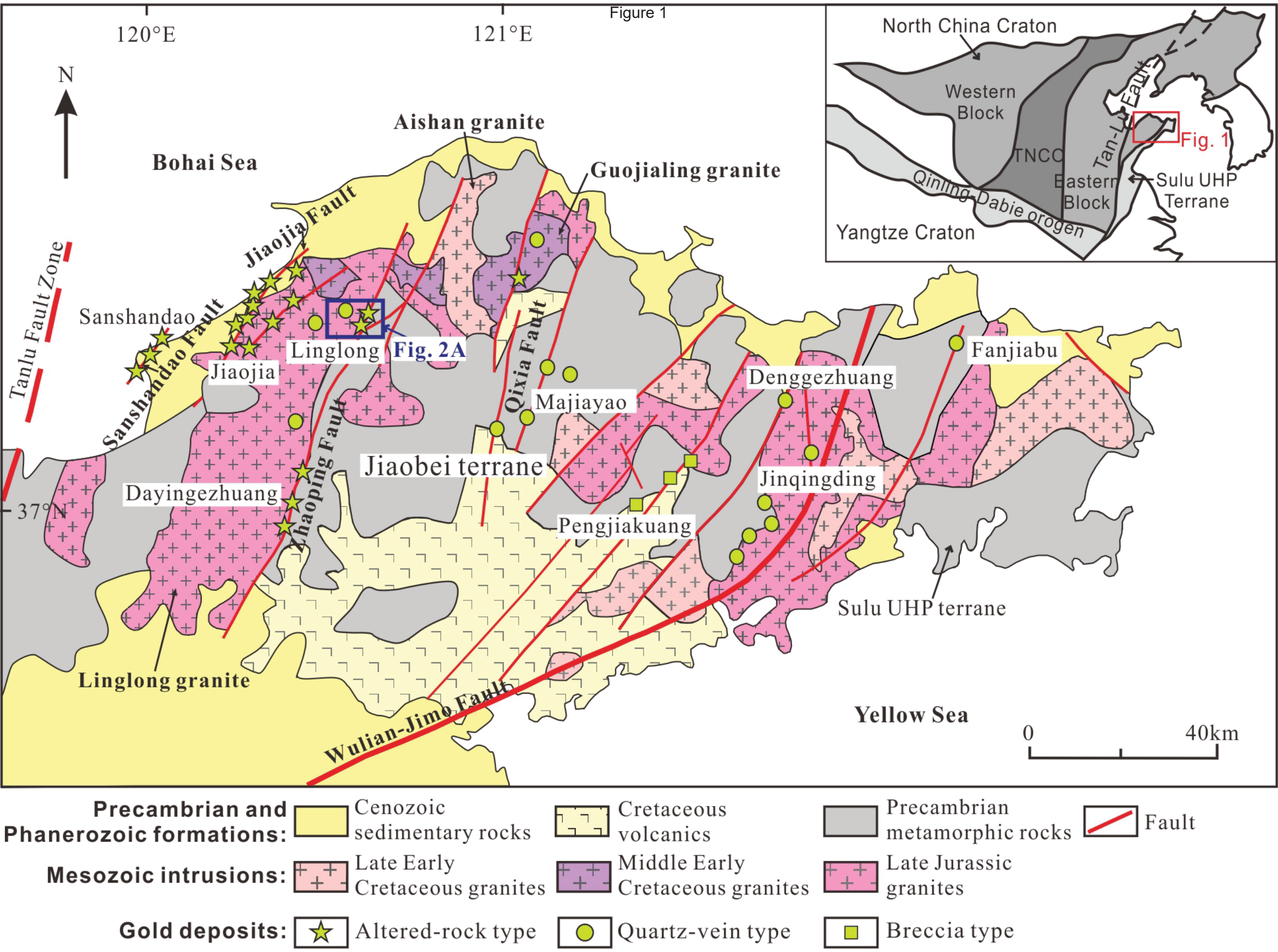

120°E
121°E
N
Bohai Sea
Aishan granite
Guojialing granite
Jiaojia Fault
Tanlu Fault Zone
Sanshandao
Sanshandao Fault
Jiaojia
Linglong
Fig. 2A
Qixia Fault
Majiayao
Denggezhuang
Fanjiabu
Zhaoping Fault
Jiaobei terrane
Dayingezhuang
37°N
Jinqingding
Pengjiakuang
Sulu UHP terrane
Linglong granite
Wulian-Jimo Fault
Yellow Sea
0
40km
North China Craton
Western Block
TNCO
Eastern Block
Tan-Lu Fault
Fig. 1
Sulu UHP Terrane
Qinling-Dabie orogen
Yangtze Craton
Precambrian and Phanerozoic formations:
Cenozoic sedimentary rocks
Cretaceous volcanics
Precambrian metamorphic rocks
Fault
Mesozoic intrusions:
Late Early Cretaceous granites
Middle Early Cretaceous granites
Late Jurassic granites
Gold deposits:
Altered-rock type
Quartz-vein type
Breccia type

Figure 2

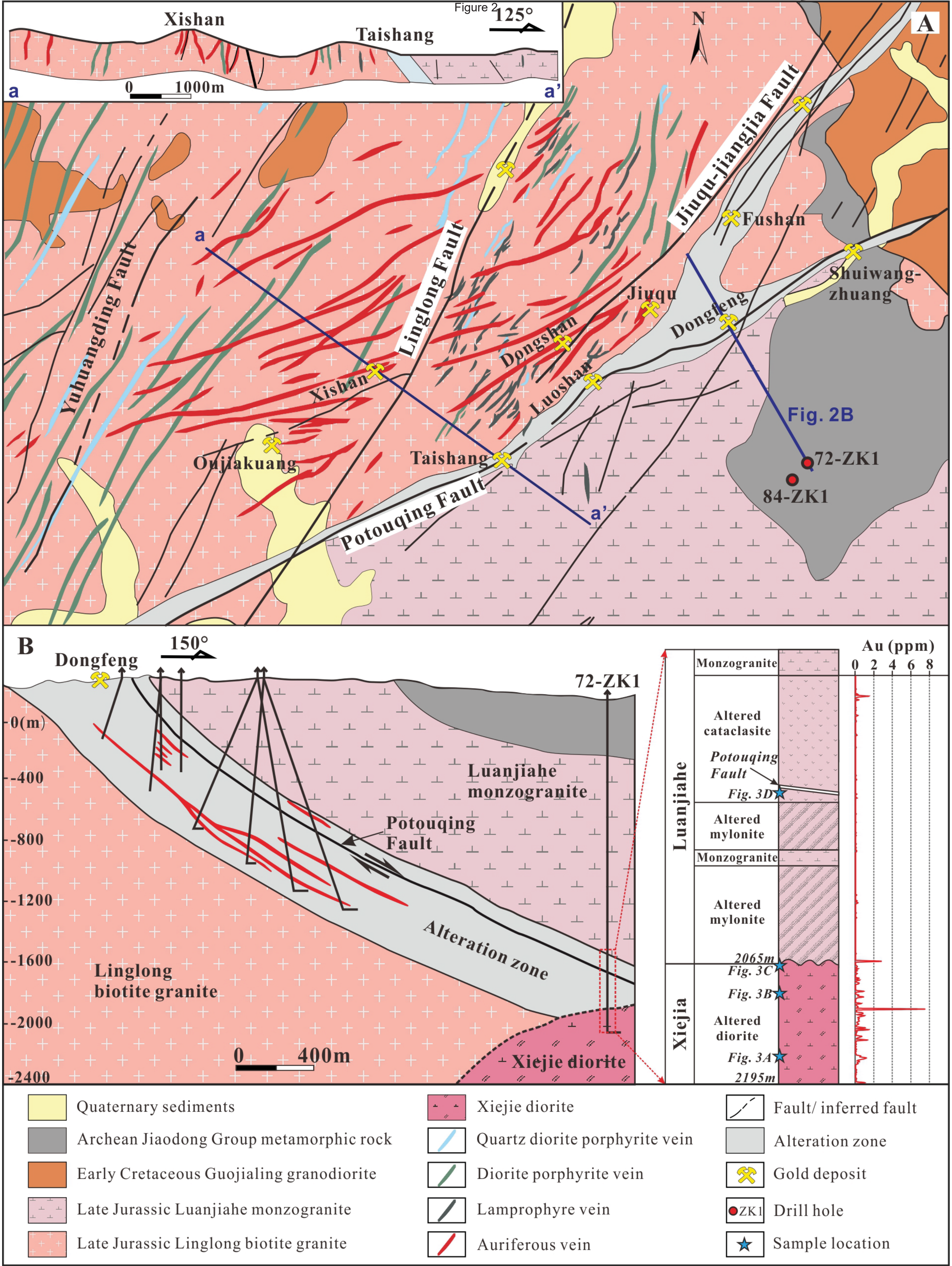

A
Xishan
Taishang
125°
a
a'
0
1000m
N
Jiuqu-jiangjia Fault
Fushan
Shuiwang-zhuang
Linglong Fault
Yuhuangding Fault
Jiuqu
Dongfeng
Dongshan
Luoshan
Xishan
Oujiakuang
Taishang
Potouqing Fault
Fig. 2B
72-ZK1
84-ZK1
B
Dongfeng
150°
72-ZK1
0(m)
-400
-800
-1200
-1600
-2000
-2400
Luanjiahe monzogranite
Potouqing Fault
Alteration zone
Linglong biotite granite
Xiejie diorite
0
400m
Luanjiahe
Xiejia
Monzogranite
Altered cataclasite
Potouqing Fault
Fig. 3D
Altered mylonite
Monzogranite
Altered mylonite
2065m
Fig. 3C
Fig. 3B
Altered diorite
Fig. 3A
2195m
Au (ppm)
0
2
4
6
8
Quaternary sediments
Archean Jiaodong Group metamorphic rock
Early Cretaceous Guojialing granodiorite
Late Jurassic Luanjiahe monzogranite
Late Jurassic Linglong biotite granite
Xiejie diorite
Quartz diorite porphyrite vein
Diorite porphyrite vein
Lamprophyre vein
Auriferous vein
Fault/ inferred fault
Alteration zone
Gold deposit
ZK1
Drill hole
Sample location

Figure 3

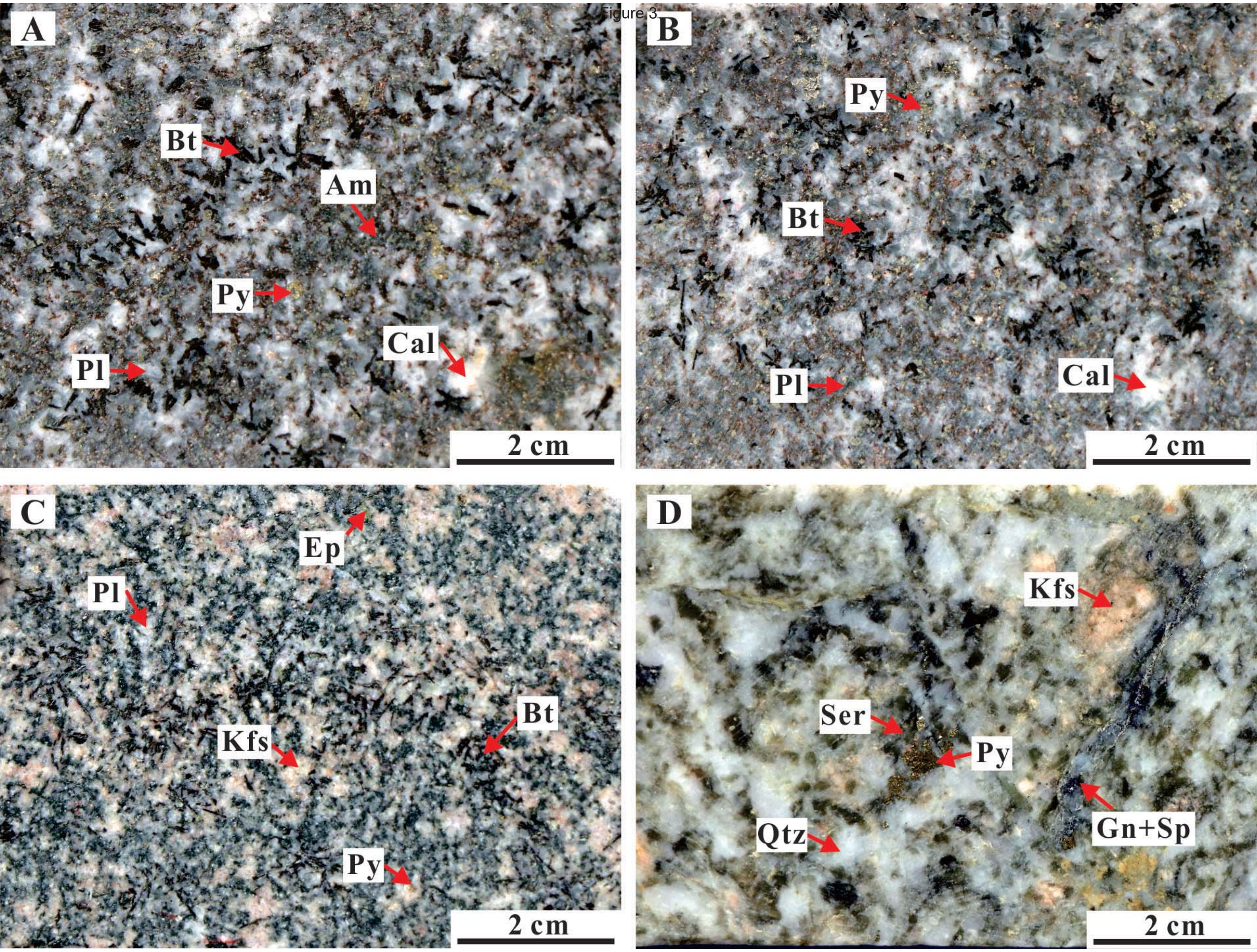
A
Bt
Am
Py
Cal
Pl
2 cm
B
Py
Bt
Pl
Cal
2 cm
C
Ep
Pl
Bt
Kfs
Py
2 cm
D
Kfs
Ser
Py
Gn+Sp
Qtz
2 cm

Figure 4

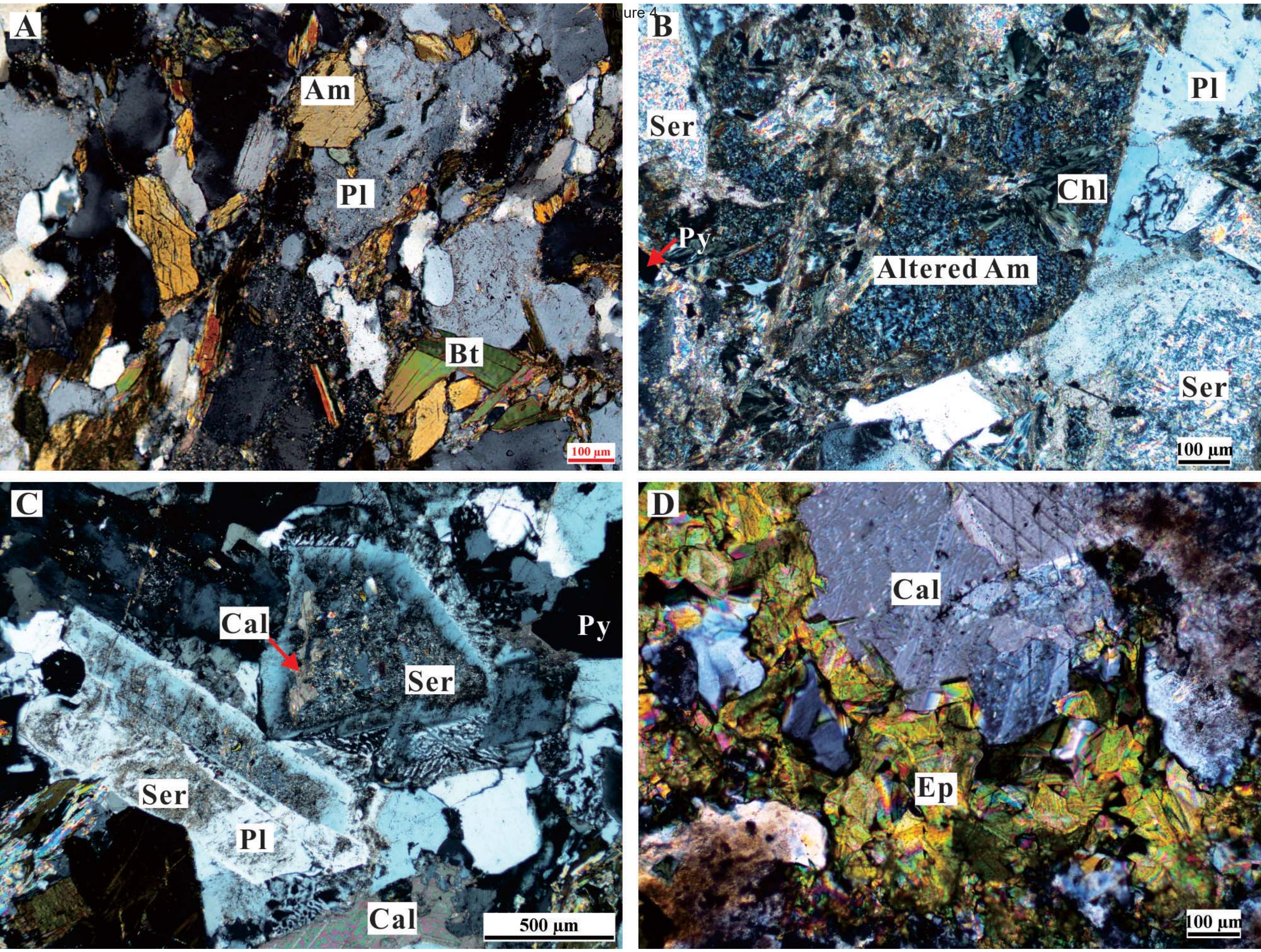
A
Am
Pl
Bt
100 μm
B
Ser
Pl
Chl
Py
Altered Am
Ser
100 μm
C
Cal
Py
Ser
Ser
Pl
Cal
500 μm
D
Cal
Ep
100 μm

Figure 5

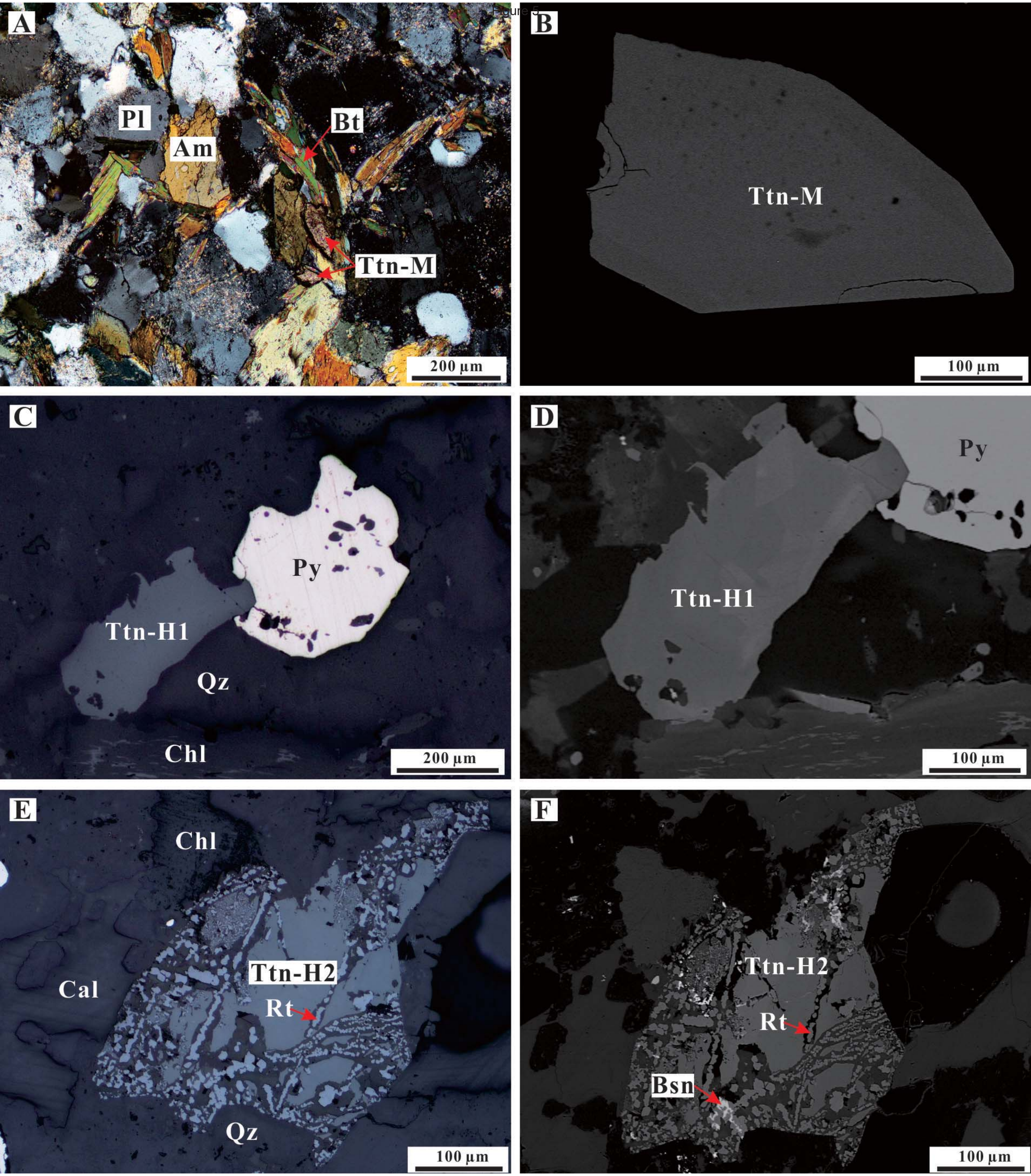

A
Pl
Am
Bt
Ttn-M
200 μm
B
Ttn-M
100 μm
C
Py
Ttn-H1
Qz
Chl
200 μm
D
Py
Ttn-H1
100 μm
E
Chl
Cal
Ttn-H2
Rt
Qz
100 μm
F
Ttn-H2
Rt
Bsn
100 μm

Figure 6

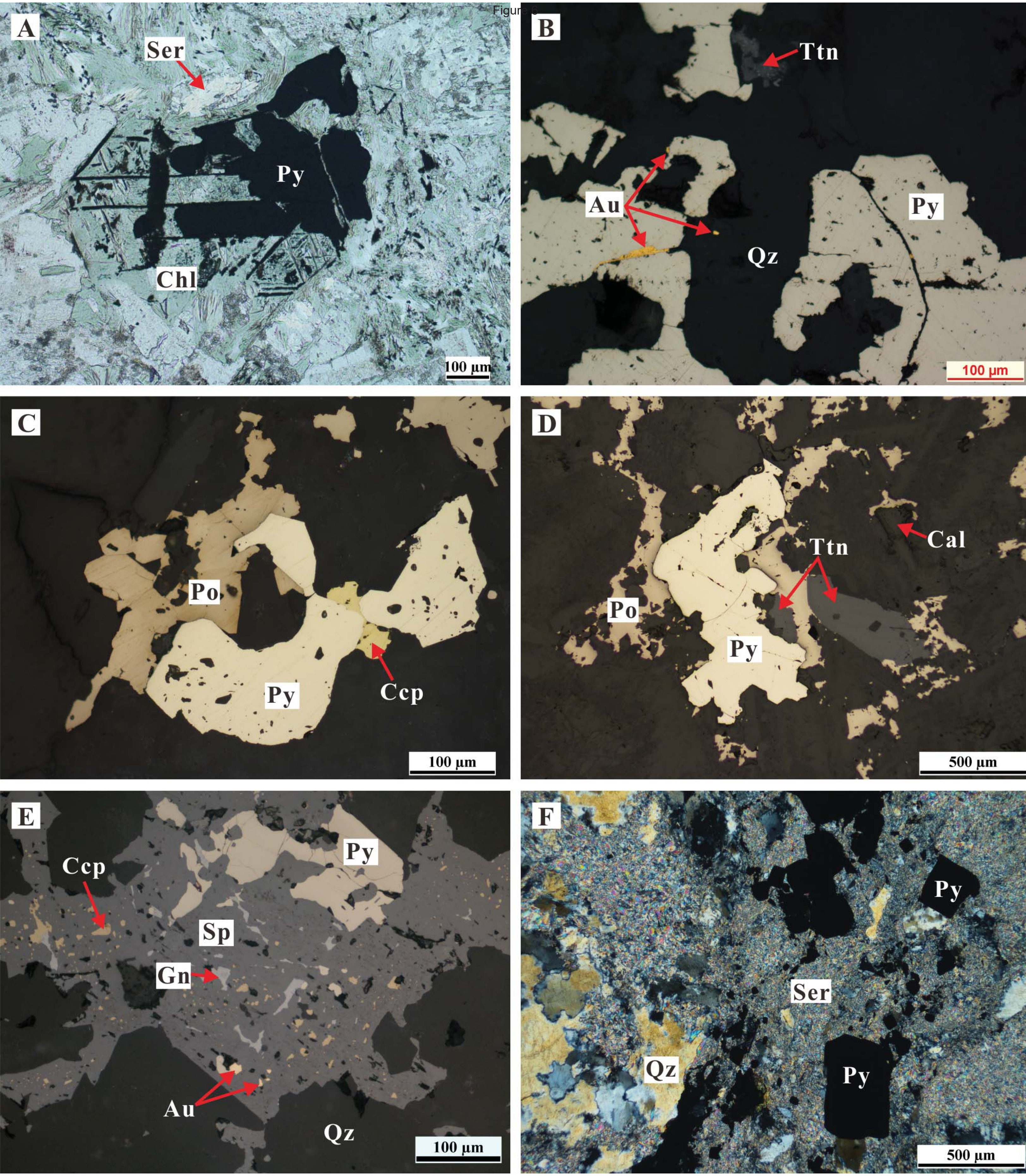
A
Ser
Py
Chl
100 μm
B
Ttn
Au
Py
Qz
100 μm
C
Po
Py
Ccp
100 μm
D
Cal
Ttn
Po
Py
500 μm
E
Py
Ccp
Sp
Gn
Au
Qz
100 μm
F
Py
Ser
Qz
Py
500 μm

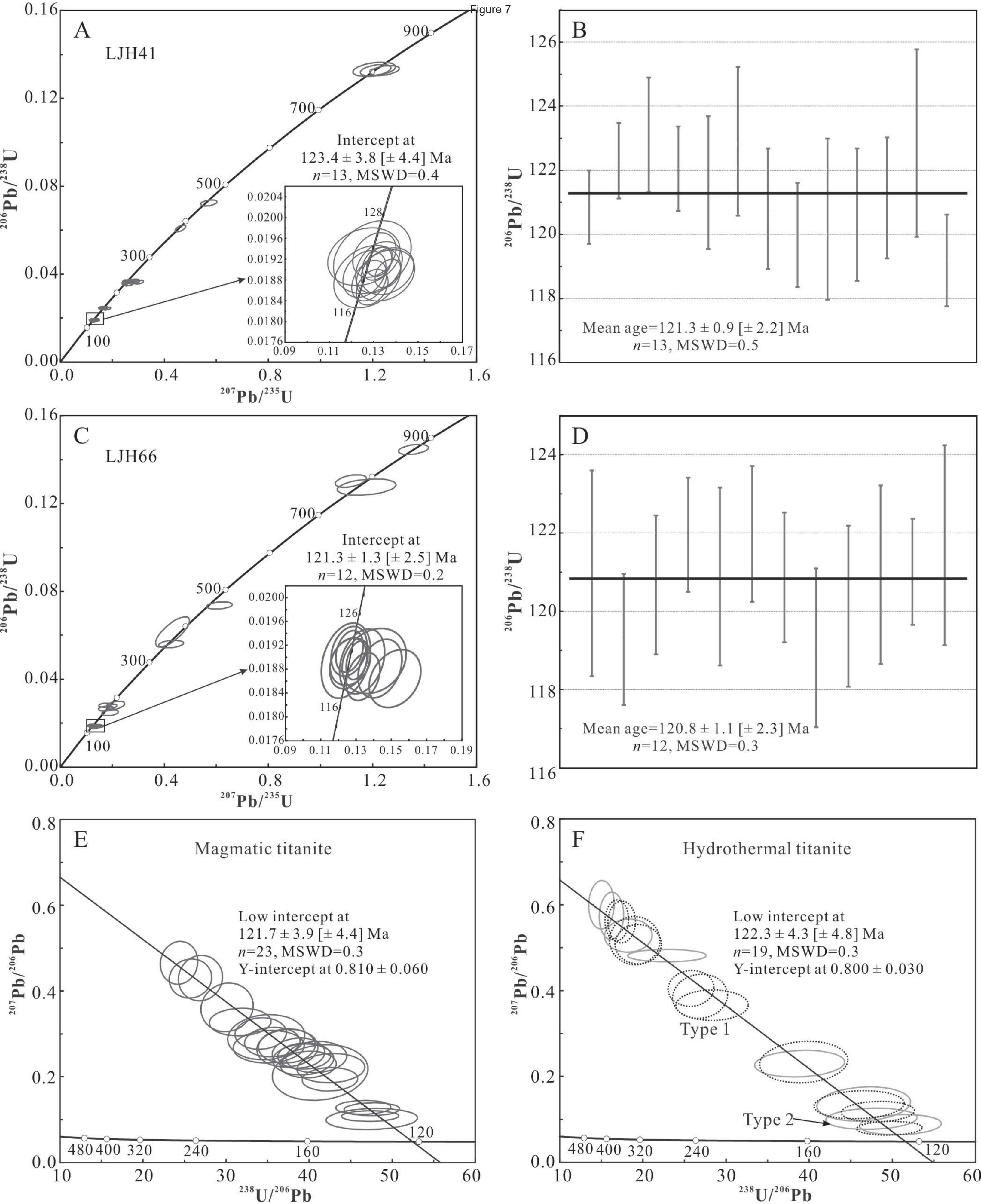
Figure 7
A
LJH41
Intercept at
123.4 ± 3.8 [± 4.4] Ma
n=13, MSWD=0.4
B
Mean age=121.3 ± 0.9 [± 2.2] Ma
n=13, MSWD=0.5
C
LJH66
Intercept at
121.3 ± 1.3 [± 2.5] Ma
n=12, MSWD=0.2
D
Mean age=120.8 ± 1.1 [± 2.3] Ma
n=12, MSWD=0.3
E
Magmatic titanite
Low intercept at
121.7 ± 3.9 [± 4.4] Ma
n=23, MSWD=0.3
Y-intercept at 0.810 ± 0.060
F
Hydrothermal titanite
Low intercept at
122.3 ± 4.3 [± 4.8] Ma
n=19, MSWD=0.3
Y-intercept at 0.800 ± 0.030
Type 1
Type 2
206Pb/238U
207Pb/235U
207Pb/206Pb
238U/206Pb

Figure 8

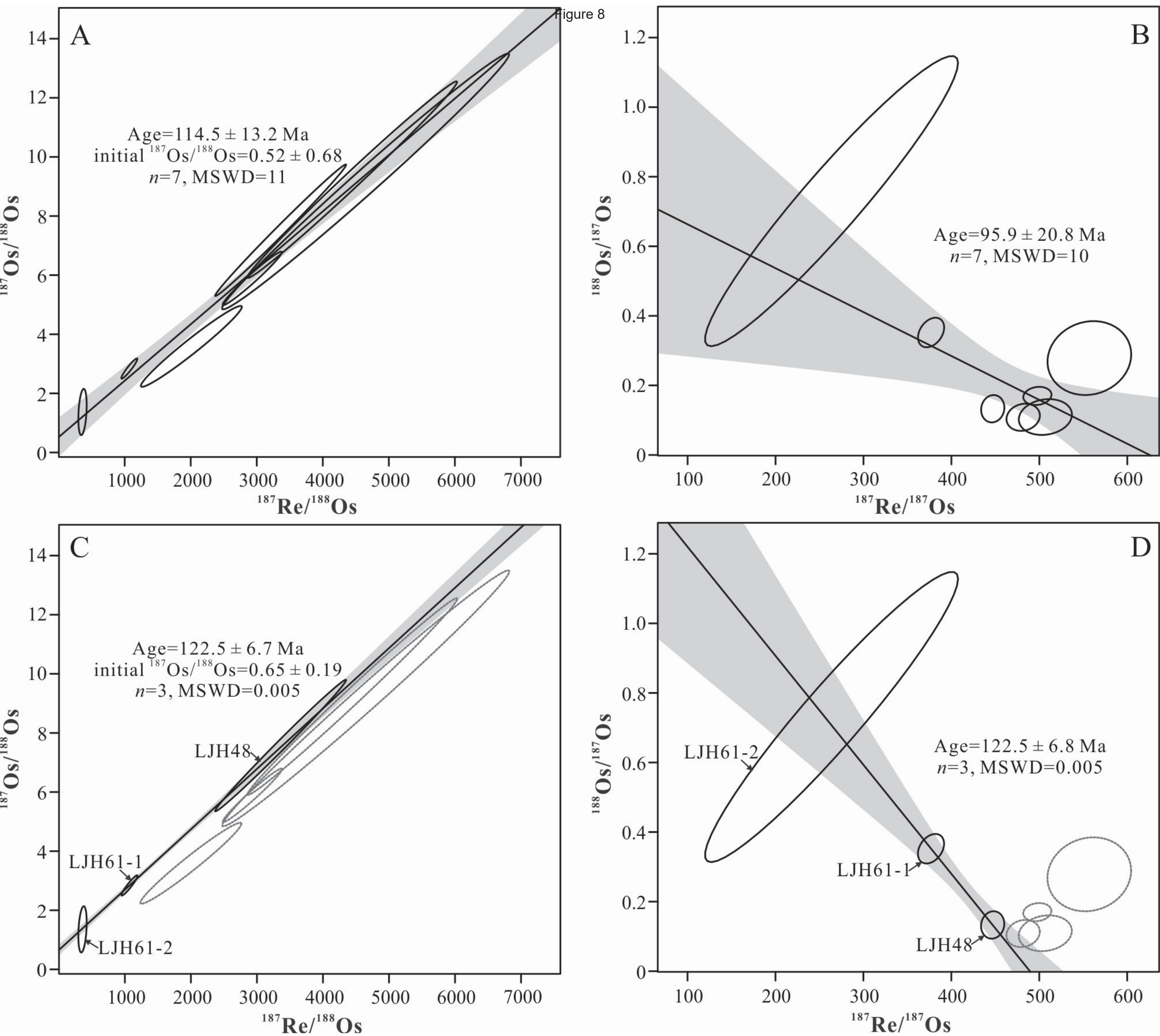
A
Age=114.5 ± 13.2 Ma
initial ¹⁸⁷Os/¹⁸⁸Os=0.52 ± 0.68
n=7, MSWD=11
187Os/188Os
187Re/188Os
B
Age=95.9 ± 20.8 Ma
n=7, MSWD=10
188Os/187Os
187Re/187Os
C
Age=122.5 ± 6.7 Ma
initial 187Os/188Os=0.65 ± 0.19
n=3, MSWD=0.005
LJH48
LJH61-1
LJH61-2
187Os/188Os
187Re/188Os
D
Age=122.5 ± 6.8 Ma
n=3, MSWD=0.005
LJH61-2
LJH61-1
LJH48
188Os/187Os
187Re/187Os

Figure 9

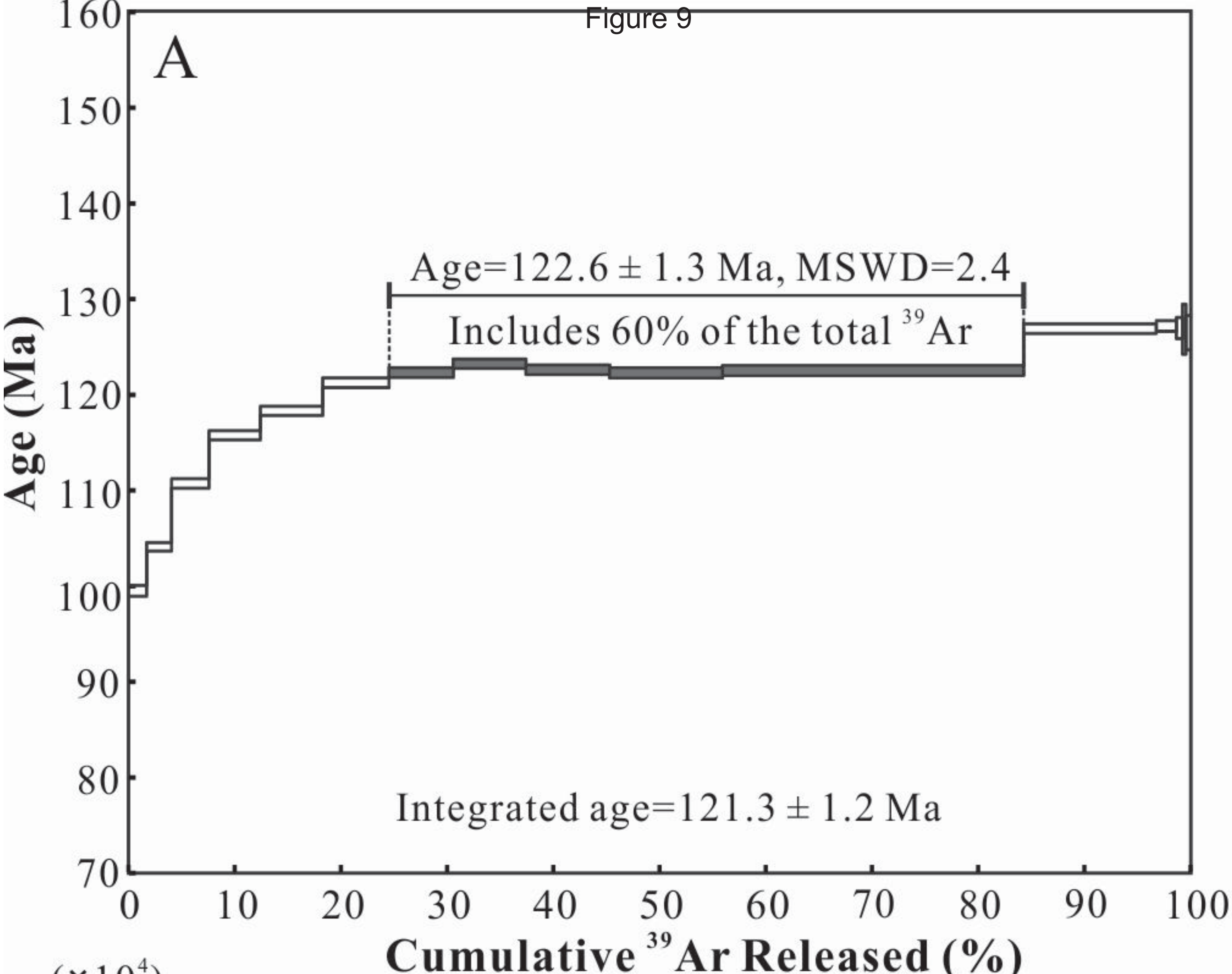

A
Age=122.6 ± 1.3 Ma, MSWD=2.4
Includes 60% of the total 39Ar
Integrated age=121.3 ± 1.2 Ma
Age (Ma)
Cumulative 39Ar Released (%)
160
150
140
130
120
110
100
90
80
70
0
10
20
30
40
50
60
70
80
90
100

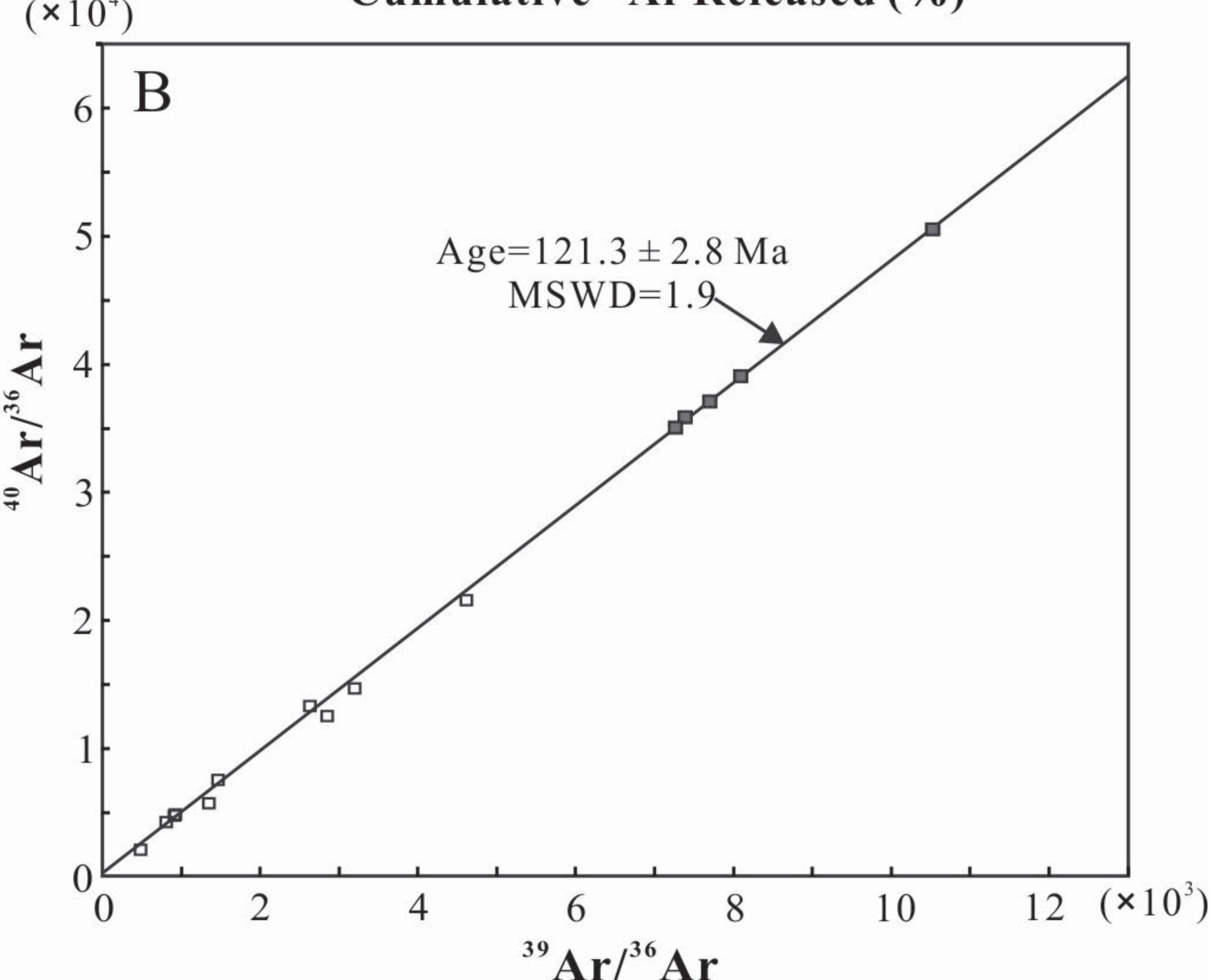

(×10^4)
B
Age=121.3 ± 2.8 Ma
MSWD=1.9
40Ar/36Ar
39Ar/36Ar
(×10^3)
6
5
4
3
2
1
0
0
2
4
6
8
10
12

Figure 10

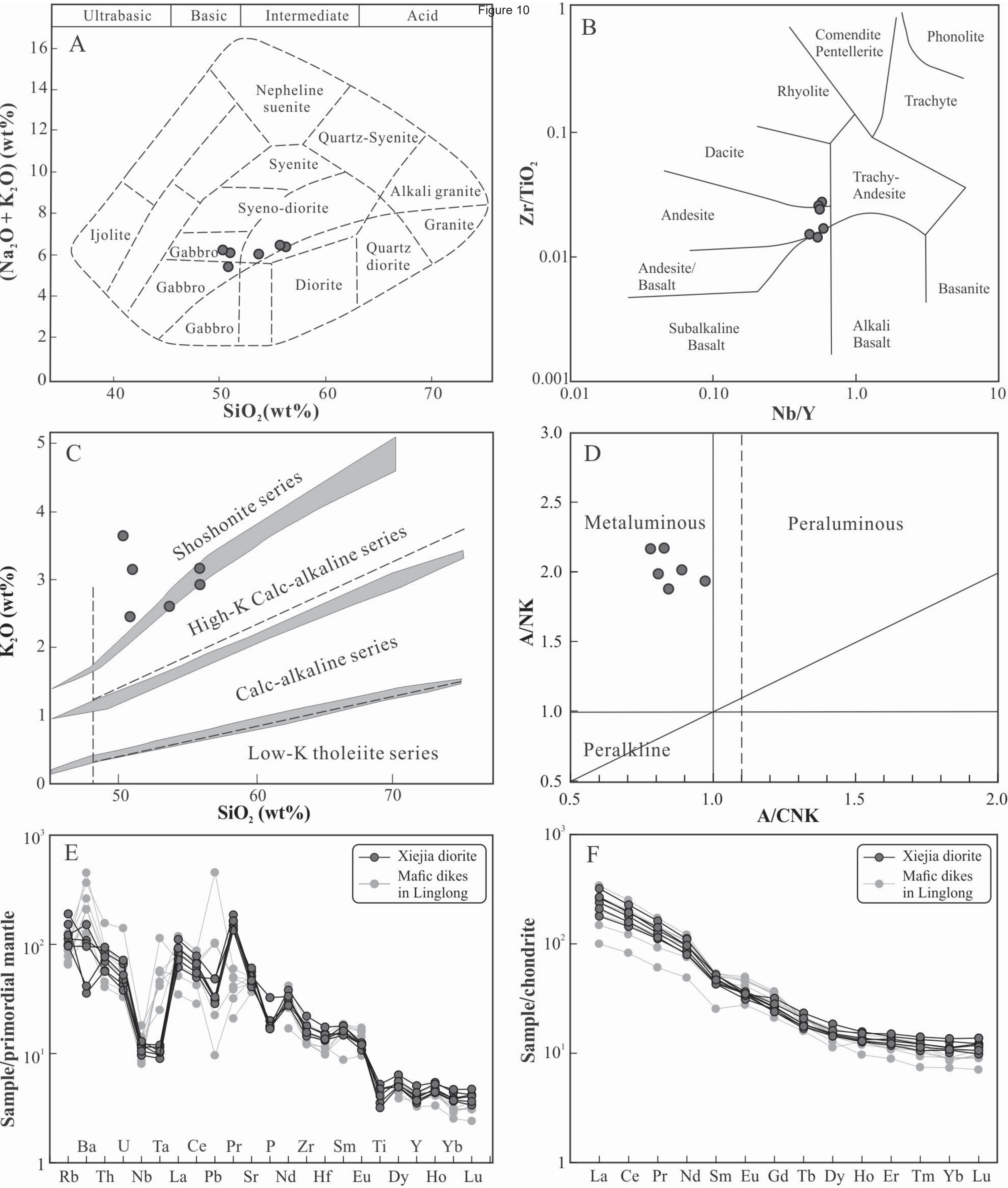
A
Ultrabasic
Basic
Intermediate
Acid
Nepheline suenite
Quartz-Syenite
Syenite
Alkali granite
Syeno-diorite
Granite
Ijolite
Gabbro
Quartz diorite
Diorite
Gabbro
Gabbro
(Na_2O+K_2O) (wt%)
SiO_2(wt%)
B
Comendite Pentellerite
Phonolite
Rhyolite
Trachyte
Dacite
Trachy-Andesite
Andesite
Andesite/Basalt
Basanite
Subalkaline Basalt
Alkali Basalt
Zr/TiO_2
Nb/Y
C
Shoshonite series
High-K Calc-alkaline series
Calc-alkaline series
Low-K tholeiite series
K_2O (wt%)
SiO_2 (wt%)
D
Metaluminous
Peraluminous
Peralkline
A/NK
A/CNK
E
Xiejia diorite
Mafic dikes in Linglong
Sample/primordial mantle
Rb Ba Th U Nb Ta La Ce Pb Pr Sr P Nd Zr Hf Sm Eu Ti Dy Y Ho Yb Lu
F
Xiejia diorite
Mafic dikes in Linglong
Sample/chondrite
La Ce Pr Nd Sm Eu Gd Tb Dy Ho Er Tm Yb Lu

Figure 11

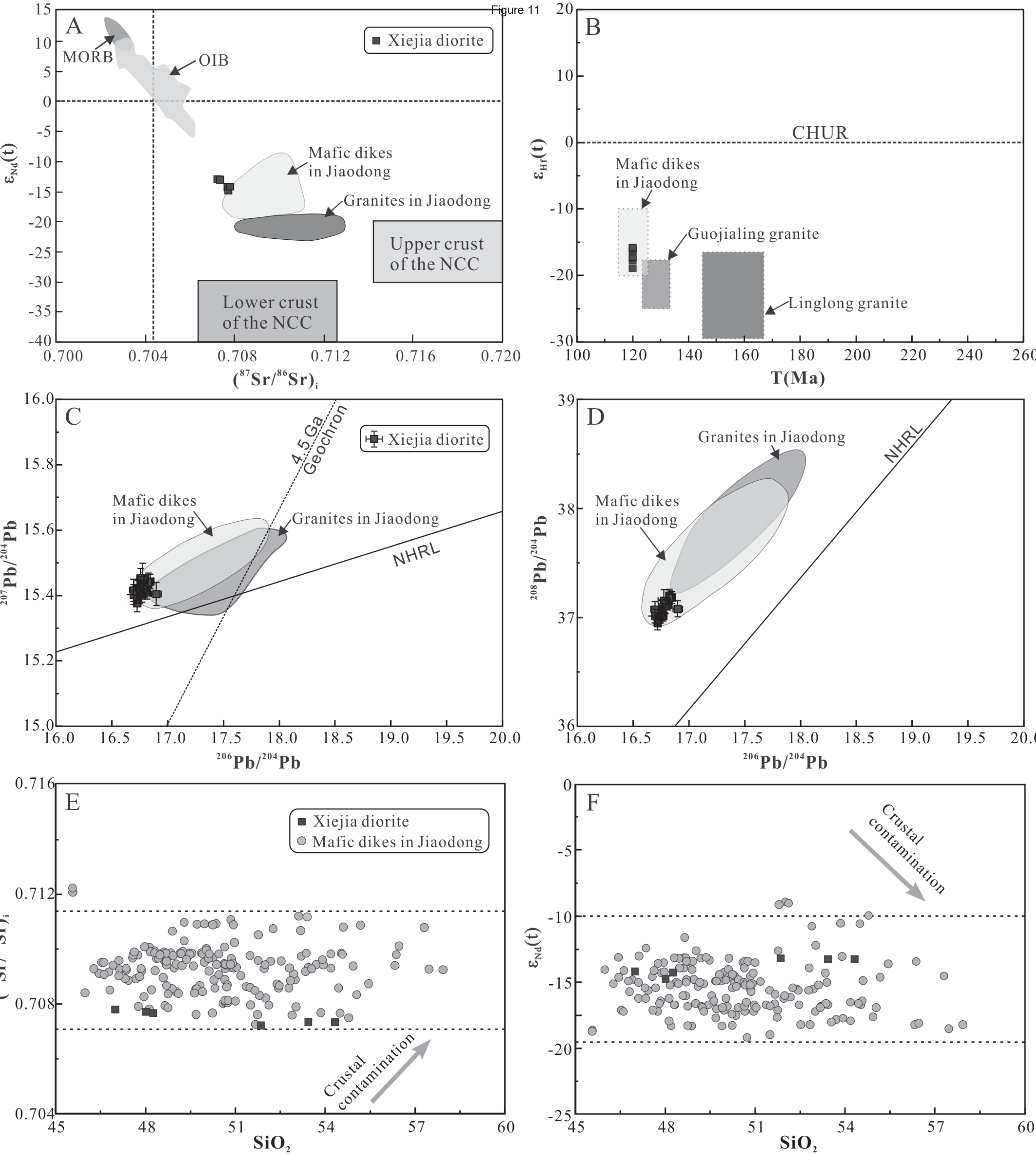

A
Xiejia diorite
MORB
OIB
Mafic dikes
in Jiaodong
Granites in Jiaodong
Upper crust
of the NCC
Lower crust
of the NCC
εNd(t)
(87Sr/86Sr)i
B
CHUR
Mafic dikes
in Jiaodong
Guojialing granite
Linglong granite
εHf(t)
T(Ma)
C
4.5 Ga
Geochron
Xiejia diorite
Mafic dikes
in Jiaodong
Granites in Jiaodong
NHRL
207Pb/204Pb
206Pb/204Pb
D
Granites in Jiaodong
NHRL
Mafic dikes
in Jiaodong
208Pb/204Pb
206Pb/204Pb
E
Xiejia diorite
Mafic dikes in Jiaodong
Crustal
contamination
(87Sr/86Sr)i
SiO2
F
Crustal
contamination
εNd(t)
SiO2

Figure 12

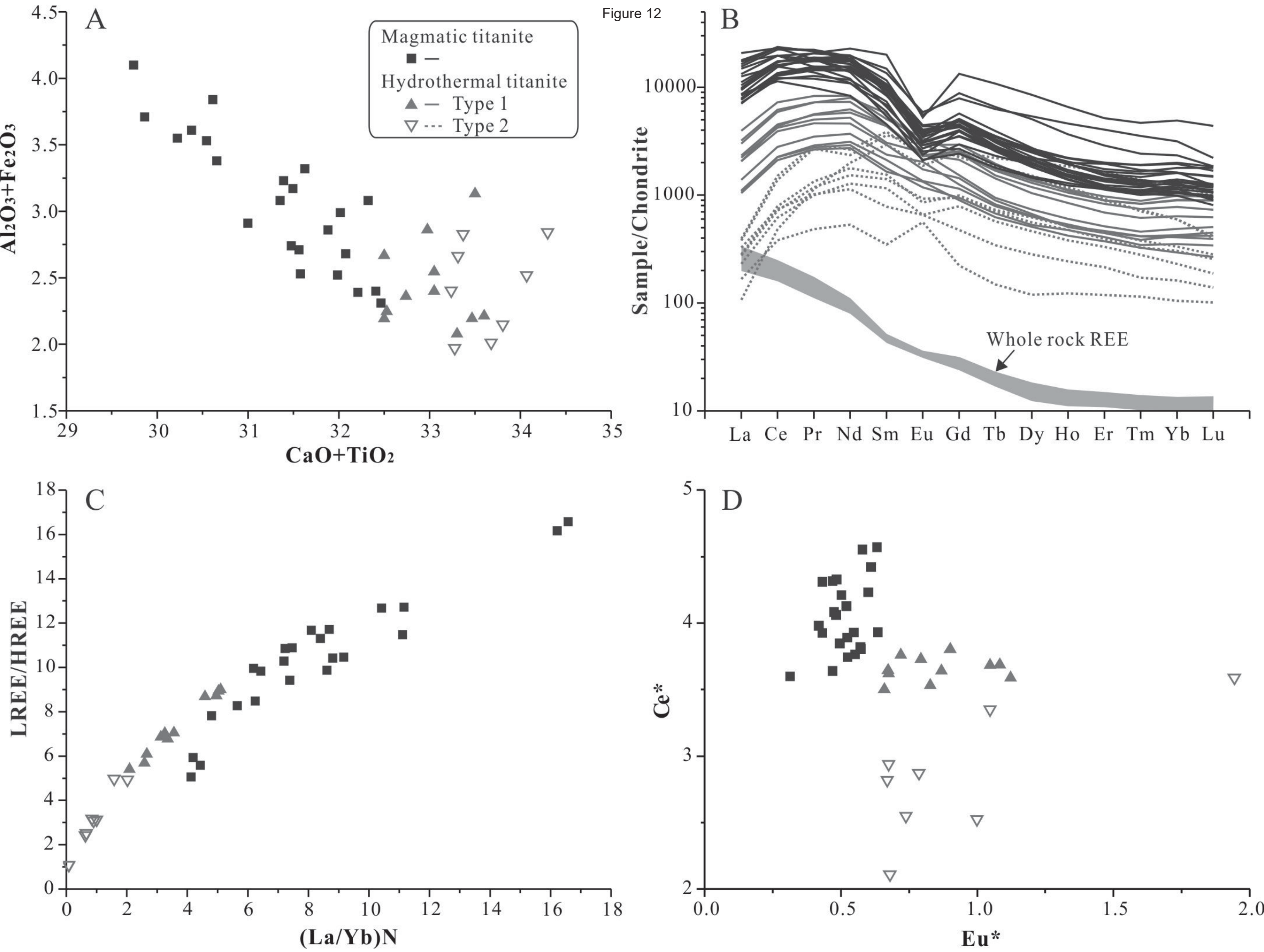

A
Magmatic titanite
Hydrothermal titanite
Type 1
Type 2
$Al_2O_3+Fe_2O_3$
$CaO+TiO_2$
B
Sample/Chondrite
Whole rock REE
La Ce Pr Nd Sm Eu Gd Tb Dy Ho Er Tm Yb Lu
C
LREE/HREE
(La/Yb)N
D
Ce*
Eu*

Figure 13

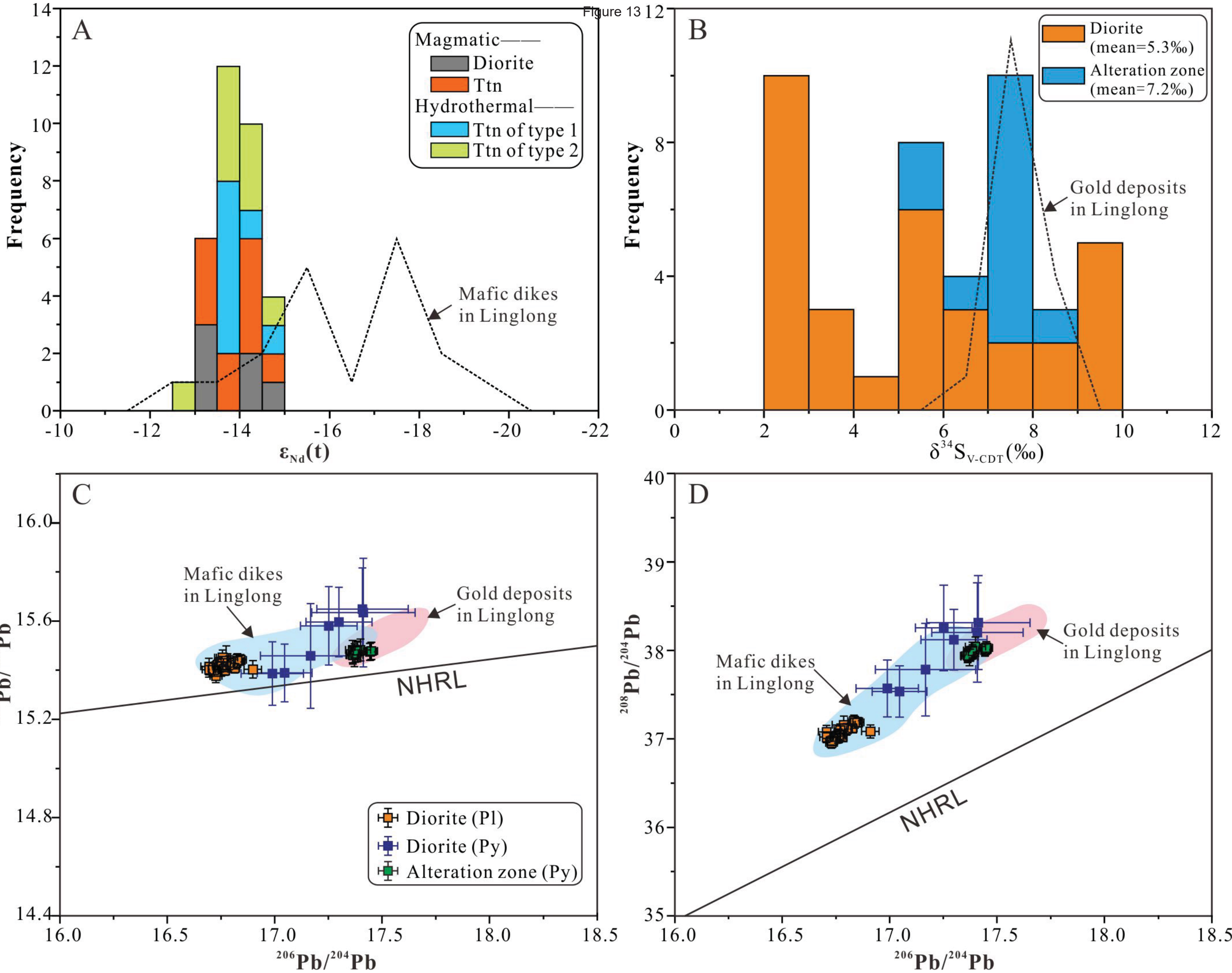

A
Magmatic——
Diorite
Ttn
Hydrothermal——
Ttn of type 1
Ttn of type 2
Mafic dikes
in Linglong
Frequency
$\varepsilon_{Nd}(t)$
B
Diorite
(mean=5.3‰)
Alteration zone
(mean=7.2‰)
Gold deposits
in Linglong
Frequency
$\delta^{34}S_{V-CDT}$(‰)
C
Mafic dikes
in Linglong
Gold deposits
in Linglong
NHRL
Diorite (Pl)
Diorite (Py)
Alteration zone (Py)
$^{207}Pb/^{204}Pb$
$^{206}Pb/^{204}Pb$
D
Gold deposits
in Linglong
Mafic dikes
in Linglong
NHRL
$^{208}Pb/^{204}Pb$
$^{206}Pb/^{204}Pb$

Figure 14

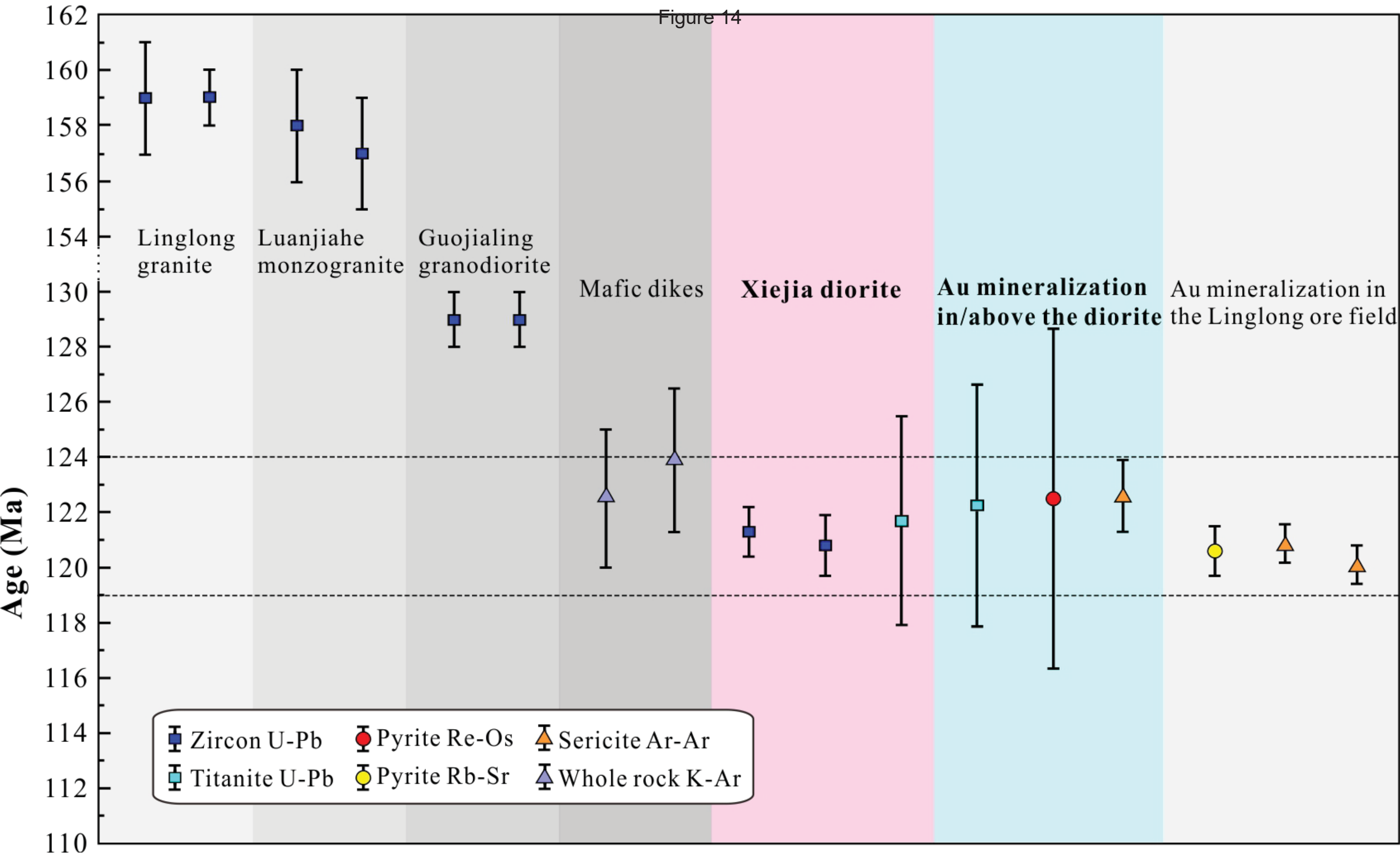
Age (Ma)
162
160
158
156
154
130
128
126
124
122
120
118
116
114
112
110
Linglong granite
Luanjiahe monzogranite
Guojialing granodiorite
Mafic dikes
Xiejia diorite
Au mineralization in/above the diorite
Au mineralization in the Linglong ore field
Zircon U-Pb
Pyrite Re-Os
Sericite Ar-Ar
Titanite U-Pb
Pyrite Rb-Sr
Whole rock K-Ar

Figure 15

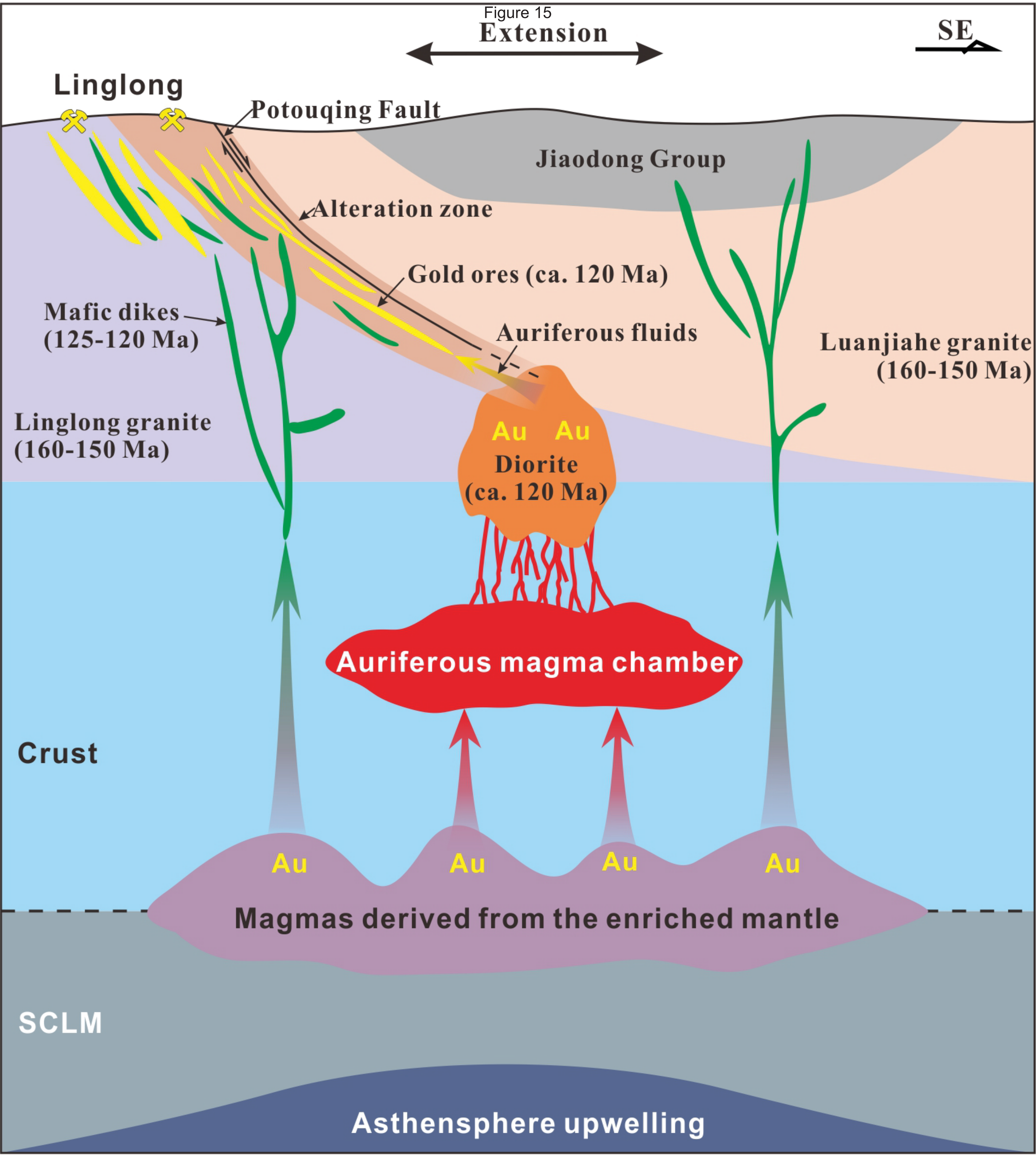
Extension
SE
Linglong
Potouqing Fault
Jiaodong Group
Alteration zone
Gold ores (ca. 120 Ma)
Mafic dikes
(125-120 Ma)
Auriferous fluids
Luanjiahe granite
(160-150 Ma)
Linglong granite
(160-150 Ma)
Au Au
Diorite
(ca. 120 Ma)
Auriferous magma chamber
Crust
Au
Au
Au
Au
Magmas derived from the enriched mantle
SCLM
Asthensphere upwelling